E
C
O
R
F
A
N

ECORFAN®

Journal - Taiwan

ECORFAN®

ECORFAN-Taiwan

ECORFAN Journal-Taiwan

Definition of Journal

Scientific Objectives

Support the international scientific community in its written production Science, Technology and Innovation in the Field of Physical Sciences Mathematics and Earth sciences, in Subdisciplines of optical astronomy, optical characterization, optical encoder, experimental research, planetary magnetic fields, ultraviolet radiation, lasers, algorithms and optical waves.

ECORFAN-Mexico, S. C. is a Scientific and Technological Company in contribution to the Human Resource training focused on the continuity in the critical analysis of International Research and is attached to CONACYT-RENIECYT number 1702902, its commitment is to disseminate research and contributions of the International Scientific Community, academic institutions, agencies and entities of the public and private sectors and contribute to the linking of researchers who carry out scientific activities, technological developments and training of specialized human resources with governments, companies and social organizations.

Encourage the interlocution of the International Scientific Community with other Study Centers in Mexico and abroad and promote a wide incorporation of academics, specialists and researchers to the publication in Science Structures of Autonomous Universities - State Public Universities - Federal IES - Polytechnic Universities - Technological Universities - Federal Technological Institutes - Normal Schools - Decentralized Technological Institutes - Intercultural Universities - S & T Councils - CONACYT Research Centers.

Scope, Coverage and Audience

ECORFAN Journal-Taiwan is a Journal edited by ECORFAN-Mexico, S. C. in its Holding with repository in Taiwan, is a scientific publication arbitrated and indexed with semester periods. It supports a wide range of contents that are evaluated by academic peers by the Double-Blind method, around subjects related to the theory and practice of optical astronomy, optical characterization, optical encoder, experimental research, planetary magnetic fields, ultraviolet radiation, lasers, algorithms and optical waves with diverse approaches and perspectives , That contribute to the diffusion of the development of Science Technology and Innovation that allow the arguments related to the decision making and influence in the formulation of international policies in the Field of Physical Sciences Mathematics and Earth sciences. The editorial horizon of ECORFAN-Mexico® extends beyond the academy and integrates other segments of research and analysis outside the scope, as long as they meet the requirements of rigorous argumentative and scientific, as well as addressing issues of general and current interest of the International Scientific Society.

Arbitration Committee

JIMENEZ - CONTRERAS, Edith Adriana. PhD
Instituto Politécnico Nacional

BELTRÁN - PÉREZ, Georgina. PhD
Instituto Nacional de Astrofísica Óptica y Electrónica

ANZUETO - SÁNCHEZ, Gilberto. PhD
Centro de Investigaciones en Óptica

GUZMÁN - CHÁVEZ, Ana Dinora. PhD
Universidad de Guanajuato

CANO - LARA, Miroslava. PhD
Universidad de Guanajuato

OROZCO - GUILLÉN, Eber Enrique. PhD
Instituto Nacional de Astrofísica Óptica y Electrónica

ROJAS - LAGUNA, Roberto. PhD
Universidad de Guanajuato

JAUREGUI - VAZQUEZ, Daniel. PhD
Universidad de Guanajuato

GARCÍA - GUERRERO, Enrique Efrén. PhD
Centro de Investigación Científica y de Educación Superior de Ensenada

GUERRERO-VIRAMONTES, J Ascención. PhD
Universidad de Guanajuato

IBARRA-MANZANO, Oscar Gerardo. PhD
Instituto Nacional de Astrofísica, Óptica y Electrónica

Assignment of Rights

The sending of an Article to ECORFAN Journal- Taiwan emanates the commitment of the author not to submit it simultaneously to the consideration of other series publications for it must complement the Originality Format for its Article.

The authors sign the Authorization Format for their Article to be disseminated by means that ECORFAN-Mexico, S.C. In its Holding Taiwan considers pertinent for disclosure and diffusion of its Article its Rights of Work.

Declaration of Authorship

Indicate the Name of Author and Coauthors at most in the participation of the Article and indicate in extensive the Institutional Affiliation indicating the Department.

Identify the Name of Author and Coauthors at most with the CVU Scholarship Number-PNPC or SNI-CONACYT- Indicating the Researcher Level and their Google Scholar Profile to verify their Citation Level and H index.

Identify the Name of Author and Coauthors at most in the Science and Technology Profiles widely accepted by the International Scientific Community ORC ID - Researcher ID Thomson - arXiv Author ID - PubMed Author ID - Open ID respectively.

Indicate the contact for correspondence to the Author (Mail and Telephone) and indicate the Researcher who contributes as the first Author of the Article.

Plagiarism Detection

All Articles will be tested by plagiarism software PLAGSCAN if a plagiarism level is detected Positive will not be sent to arbitration and will be rescinded of the reception of the Article notifying the Authors responsible, claiming that academic plagiarism is criminalized in the Penal Code.

Arbitration Process

All Articles will be evaluated by academic peers by the Double Blind method, the Arbitration Approval is a requirement for the Editorial Board to make a final decision that will be final in all cases. MARVID® is a derivative brand of ECORFAN® specialized in providing the expert evaluators all of them with Doctorate degree and distinction of International Researchers in the respective Councils of Science and Technology the counterpart of CONACYT for the chapters of America-Europe-Asia- Africa and Oceania. The identification of the authorship should only appear on a first removable page, in order to ensure that the Arbitration process is anonymous and covers the following stages: Identification of the Journal with its author occupation rate - Identification of Authors and Coauthors - Detection of plagiarism PLAGSCAN - Review of Formats of Authorization and Originality-Allocation to the Editorial Board-Allocation of the pair of Expert Arbitrators-Notification of Arbitration -Declaration of observations to the Author-Verification of Article Modified for Editing-Publication.

Instructions for Scientific, Technological and Innovation Publication

Knowledge Area

The works must be unpublished and refer to topics of optical astronomy, optical characterization, optical encoder, experimental research, planetary magnetic fields, ultraviolet radiation, lasers, algorithms and optical waves and other topics related to Physical Sciences Mathematics and Earth sciences.

Presentation of the content

In the first article we present, *Numerical analysis of the hydrodynamic behavior of a magnetoreological fluid*, by ORTEGA-ROMERO, Daysi Flor de Liz, ZÚÑIGA-CERROBLANCO, José Luis and HORTELANO-CAPETILLO, Juan Gregorio, with adscription in the Universidad Politécnica de Juventino Rosas, in the next article we present, *Automatic blood vessel detection using fractional Hessian matrices*, by MARTÍNEZ-JIMÉNEZ, Leonardo, LÓPEZ-LARA, Pedro, FLORES-BALDERAS, Adán and LÓPEZ-HERNÁNDEZ, Juan Manuel, with adscription in the Universidad de Guanajuato, in the next article we present, *Use of unstructured meshes for wave height and particles horizontal displacement analysis in central zone Veracruz, Mexico*, by AGUILERA-MENDEZ, José María, JUAREZ-TOLEDO, Carlos, MARTINEZ-CARRILLO, Irma and VERA-POPOCA, Roberto Ismael, with adscription in the Universidad Autónoma del Estado de México, in the last article we present, *BFO films obtained by Spray Pyrolysis optical and structural analysis*, by HERNÁNDEZ-SIMÓN, Zaira Jocelyn, LUNA-LÓPEZ, José Alberto, HERNÁNDEZ-DE LA LUZ, Álvaro David and MENDOZA-CONDE, Gabriel Omar, with adscription in the Benemérita Universidad Autónoma de Puebla.

Content

Article	Page

Numerical analysis of the hydrodynamic behavior of a magnetoreological fluid

Análisis numérico del comportamiento hidrodinámico de un fluido magnetoreológico

ORTEGA-ROMERO, Daysi Flor de Liz†*, ZÚÑIGA-CERROBLANCO, José Luis and HORTELANO-CAPETILLO, Juan Gregorio

Universidad Politécnica de Juventino Rosas. Master's Degree in Engineering, Mexico.

ID 1sr Author: *Daysi Flor de Liz, Ortega-Romero* / **ORC ID:** 0000-0001-7364-4729, **CVU CONACYT ID:** 1198186

ID 1st Co-author: *José Luis, Zúñiga-Cerroblanco*/ **ORC ID:** 0000-0003-0493-8197

ID 2nd Co-author: *Juan Gregorio, Hortelano-Capetillo*/ **ORC ID:** 0000-0002-3702-4853

Abstract

In this work, a numerical analysis of the behavior of magnetorheological fluids under the influence of different magnitudes of magnetic field is carried out. The properties of these fluids are affected and modified through the application of these magnetic fields, which has many applications in the engineering area. To carry out the analysis, a circular geometry is taken on which the magnetic field acts perpendicular to the direction of movement of the fluid. The magnetorheological fluid used is Basonetic 5030. The inlet velocity of the fluid is considered to be 1.31 m/s for the geometry of 20 and 30 mm, respectively. The Bingham viscosity model is used to obtain the viscosity. For the numerical solution is used a commercial software, in which has been used a UDF for the application of the Bingham viscosity model. Among the reported results is the velocity profile and the pressure drop along the duct for magnetic fields of 0.01 to 0.5 Teslas, here is observed the influence of the magnetic effects on the magnetorheological fluid with different diameters.

Resumen

En el presente trabajo se lleva a cabo un análisis numérico del comportamiento de fluidos magnetoreológicos bajo la influencia de diferentes magnitudes de campo magnético. Las propiedades de estos fluidos se ven afectadas y modificadas mediante la aplicación de dichos campos magnéticos, lo cual tiene diversas aplicaciones en el área de ingeniería. Para realizar el análisis, se toma una geometría de forma circular sobre la cual actúa el campo magnético perpendicular a la dirección del movimiento del fluido. El fluido magnetoreológico que se utiliza es Basonetic 5030. La velocidad de entrada del fluido se considera de 1.31 m/s para la geometría de 20 y 30 mm, respectivamente. Se utiliza el modelo de viscosidad de Bingham para la obtención de la viscosidad. Para la solución numérica se utiliza un software comercial, en el cual se ha usado un UDF para la aplicación del modelo de viscosidad Bingham. Dentro de los resultados que se reportan está el perfil de velocidad y la caída de presión a lo largo del ducto para el rango de campos magnéticos de 0.01 a 0.5 Teslas, aquí se observa la influencia de los efectos magnéticos sobre el fluido magnetoreológico con diferente diámetro.

Magnetorheological fluid, Magnetic field, Computational Fluid Mechanics (CFM)

Fluido magnetoreológico, Campo magnético, Mecánica de Fluidos Computacional (CFD)

Introduction

Magnetorheological fluids (MRFs) are dispersions of granular particles in a carrier liquid such as water, mineral oil and hydrocarbon-based oils(Çeşmeci, Ş., & Engin, 2010; Susan-Resiga, D., Bica, D., & Vékás, 2010). The particle diameter of these suspensions varies between 1 and 5 μm.

These fluids when in the absence of a magnetic field behave as a Newtonian fluid since their viscosity remains constant. However, when the fluid is exposed to a magnetic field, its properties change causing an alignment of the particles in the direction of the applied field forming chains where it acquires an increase in its viscosity, acquiring a non-Newtonian behavior and becomes a semi-solid state as can be seen in Figure 1.
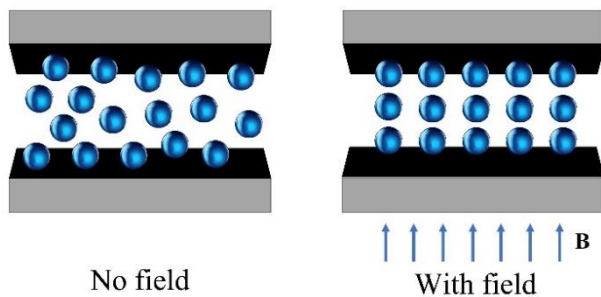
Figure 1 Formation of chains of particles suspended from an MR fluid by the presence of an external magnetic field
Source: Own elaboration

The main applications of FMRs are developed in different industrial products, i.e., from clutches, shock absorbers, valves and seals, to biomedical applications, mainly in prosthetics and cancer treatment. However, one of the disadvantages is particle sedimentation, so studies have focused on the chemical stability of these fluids.

As the viscosity of the fluid increases, the yield stress $\tau 0$ also changes. This behavior of the MR fluid corresponds to the Bingham model, as can be seen in Figure 1, which is characterized by yield stresses in relation to the intensity of the applied magnetic field. This effect is achieved because when a magnetic field is induced, the chains formed restrict the movement of the fluid, changing its rheological properties; when the field is removed, this effect disappears, returning to its initial state (Phule, 2001).

Graphic 1 Behavior of an idealized Bingham model, MR fluid in the presence of an applied magnetic field (H) as a function of shear rate
Source: Own elaboration
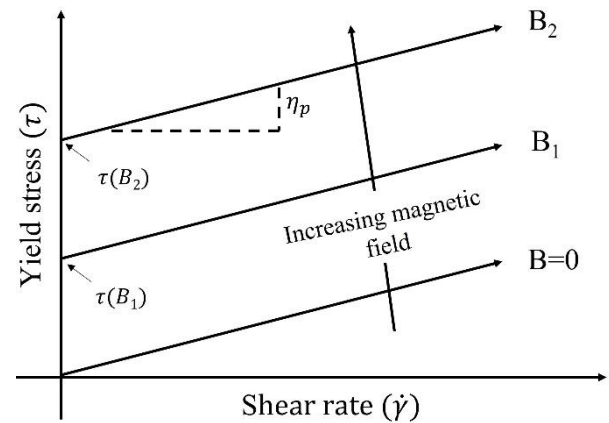
Background

Due to the viscous behavior of MR fluids when exposed to a magnetic field, it is possible to make devices with smaller size, but with a wide range of service (Yang, 2002), this is due to the fact that MR fluids have a facility to generate a magnetic saturation of particles.

Due to the rheological properties of MR fluids, these fluids have been implemented in several applications, mainly in the engineering area. The best known devices with MR fluids are shock absorbers that can currently be found in luxury(Bai, X-X, Chen, P, Qian, 2015; Bai, X-X, Hu, W, Wereley, 2013; Boada, MJ, Calvo, JA, Boada, BL, et, 2011; Chae, HD, Choi, 2015; Gurubasavaraju, M, Kumar, H, Mahalingam, 2018), in which there is a rapid response in controlling vibrations and oscillations resulting from walking improving vehicle stability.

Research is also being conducted regarding the use of MR fluids in dampers used for building and bridge foundations (Ding, Y, Zhang, L, Zhu, H-T, et, 2013; Wu, 2010), railway suspension (Kim, H-C, Shin, Y-J, You, W, et, 2016) for the protection of these against earthquakes as it absorbs vibrations produced during these natural phenomena, they can also be found in tracked vehicles such as military and agricultural trucks (Ata, WG, Oyadiji, 2014), in the medical area have been investigated prostheses in which motors will be eliminated and therefore decreases its weight since the size of the prosthesis is reduced obtaining the same or even better performance and response time compared to other prostheses, strength is provided to the fingers or arm, in the case of leg prosthesis, it improves the walking gait, which benefits the individuals who use it, since they have a more uniform gait and therefore will not have a hip deformity as a consequence of using a prosthesis (Case, D, Taheri, B, Richer, 2014; Qiang, F, Wang, D-H, Lei, X, et, 2017), and in recent years, MR dampers were investigated to incorporate features to make it more functional, also it has attracted more interest recently in studying the damping force in MR dampers (Deng, L, Sun, S, Christie, MD, et, 2019; Huang, H, Sun, S, Chen, S, et, 2019).

Various authors have proposed several theoretical models to predict the behavior of MR fluids and each of these may be more precious than the other, however, to select one of these models should consider the mode of operation and the type of device in which it will be used.

Wang and (Liao, 2011), studied different parametric models of MR dampers, dynamic models based on Bingham, bi-viscous model and the Bouc-Wen model, upon comparison in the results obtained the Bingham dynamic model is preferred compared to the two quasi-static models due to the fact that with the dynamic model the hysteretic behavior of MR dampers can also be predicted.

Although a wide variety of rheological models have been studied to describe the behavior of MR fluids, it should be considered that the Bingham and Herschel-Bulkley models are the most widely used due to their simplicity compared to other models; however, if these two models are compared it is more appropriate to use the Herschel-Bulkley model in the case of high values in shear stress.

(Omidbeygi F, 2012) used the Herschel-Bulkley model to study the hydrodynamic characteristics of an MR fluid inside a rotational eccentric cylinder in a shear mode, results of good fluid consistency at high shear rates over a wide range of magnetic field strengths were obtained, to validate these results were compared analytically and numerically.

(Goldasz J, 2012) used the Bingham, bi-viscous and Herschel-Bulkley models to analyze the flow behavior of an MR fluid in a damper, the results obtained analytically were compared with experimental results and a good consistency and lower margin of error was obtained between the results obtained with the Herschel-Bulkley model and the experimental data.

The study of MR solutions in Poiseuille or capillary flow, there are very few works. One of them is the work of (Wang, X., & Gordaninejad, 2006) in which they performed a study of magnetorheological fluids at high shear values for three magnetorheological fluids (MRF-132LD, PAO MRPG, Ferro-MRF), with iron particles. These authors designed a viscometer where the flow was generated by the movement of a piston and in this way they controlled the speed of deformation, to store the fluid they used an accumulator and applied an external magnetic field only in a part of the channel. They found that the fluids show a non-Newtonian thinning behavior and an increase in viscosity with increasing magnetic field.

(Gedik, 2017), conducted a study comparing the results obtained experimentally and numerically of magnetorheological fluids located in a circular pipe under the influence of different magnetic field strengths, where it was shown that as the magnetic field increases the velocity decreases as the viscosity increases which results in an increase in pressure. When making the comparisons between the experimental and numerical study, the results have a variation of 6.10% when the fluid is without field and 1.71% when the field is applied, this for a 10 mm diameter pipe; however, for the 15 mm pipe a variation of the results of 2.31% without field and 0.89% when applying magnetic field was obtained. By having a very low margin of error, it shows that the results obtained from the numerical and experimental parts agree.

(Pappas, Y., & Klingenberg, 2006), performed a simulation with Poiseuille geometry, i.e., of the flow of an MR fluid generated by a pressure gradient moving between two parallel magnetizable plates, the fluid is composed of dispersed particles floating in a continuous phase of Newtonian behavior, the magneto-static force was treated in the limit of the dipole point. Applying two different boundary conditions; in the first case, a no-slip and frictionless condition is considered. For this case, they found that the inclusion of friction reproduces the behavior of a Bingham fluid, which was expected to be obtained according to what was observed experimentally for MR fluids. In addition, the formation of laminar structures after the yield region was found. For the second case, the slip boundary condition produces higher flow velocities compared to the first case and thicker laminar structures, but does not reproduce the Bingham behavior, since no yield stress is present. However, for both cases the presence of velocity fluctuations is obtained. These are associated with changes in the microstructure of the fluid, where the chains are continuously broken and reformed.

One of the main advantages of using computational software for the solution of the governing equations is that the analysis can be carried out in 3D and the continuity, momentum and energy equations can be solved together.

CFD is used to simulate both laminar and turbulent fluid flows. However, there is no software that can accurately simulate a magnetorheological fluid. Therefore, existing software must be complemented, either by incorporating user-defined functions to achieve an accurate simulation of magnetorheological fluids.

In this work a numerical study of an incompressible MR fluid under a laminar regime is carried out, this fluid is conducted through a cylindrical pipe, for which a diameter of 10 and 15 mm is considered, this pipe is exposed in a section to an external and uniform magnetic field, which is applied perpendicular to the direction of flow. Computational Fluid Dynamics (CFD) analysis was used to carry out the numerical study.

Development

Geometry

Figure 2 shows the schematic representation of the pipe geometry used for the numerical analysis. Two circular geometries were made, in which, diameters of 20 and 30 mm with a length of 300 mm are considered for both cases. The flow model geometry and mesh were designed in ICEM CFD and then exported to ANSYS-Fluent for the 3D laminar flow solution.
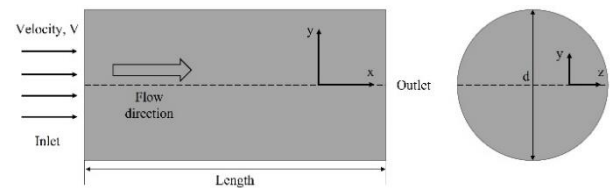
Figure 2 Schematic view of the pipe geometry used in CFD simulations
Source: Own elaboration

Materials

In this study, an MR fluid, which is Basonetic 5030, is analyzed. The MR fluid analyzed is a sample with 20% volumetric concentration of carbonyl iron powder diluted in an alpha-type polyolefin base fluid. This fluid is used for all numerical studies and its physical properties are given in Table 1. A rheometer was used to determine the viscosity of the MR fluid. As a result of the viscosity measurement, a value of 0.909 Pas was obtained at a temperature of 40°C and a shear rate of 99.55 1/s without applying a magnetic field strength.

	Basonetic 5030
Density (g/cm^3)	1.8
Viscosity (Pas, measured at 40 °C, γ=99.55 1/s)	0.909
Concentration (%)	20
Base fluid	Poly-α-olefin
Magnetizable particle	Carbonyl Iron Powder
Temperature range (°C)	-40 °C to +120 °C

Table 1 Physical properties of MR fluid
Source:(Gedik, 2017)

ORTEGA-ROMERO, Daysi Flor de Liz, ZÚÑIGA-CERROBLANCO, José Luis and HORTELANO-CAPETILLO, Juan Gregorio. Numerical analysis of the hydrodynamic behavior of a magnetoreological fluid. ECORFAN Journal-Taiwan. 2022

Mesh analysis

The generation of the geometry mesh is performed by means of a structured meshing which has as primary objective the calculation of the position of the nodes in the geometry, so that the resulting elements present certain characteristics of size and regularity, for the meshing method, a tetrahedral method is selected, with BiGeometric mesh law with variations in the number of nodes in the geometry. The information of the mesh convergence study for the 20 and 30 mm diameter pipe geometry is provided in Table 2.

Diameter (mm)	Length (mm)	Number of mesh	Number of nodes	Average speed (m/s)
10	300	1a	24000	1.0338
		2a	25780	1.3483
		3a	106600	1.1928
		4a	553200	1.4903
		5a	127200	1.6629
		6a	1279200	1.3077
		7a	223500	1.6706
		8a	302700	1.6365
		9a	444000	1.5477
		10a	739500	1.4038
		11a	952800	1.3579
		12a	1193100	1.3196
5		1b	127200	2.8359
		2b	223500	2.8438
		3b	302700	2.8323
		4b	444000	2.8032
		5b	553200	2.7597
		6b	739500	2.6594
		7b	952800	2.4705
		8b	1110000	2.1954
		9b	1279200	1.5038

Table 2 Mesh convergence information
Source: Own elaboration

In addition, the software tool chosen to mesh the model is an important decision; accuracy, flexibility and ease of use are important features to choose the most suitable one. The mesh developed for this model has been designed with the commercial software ICEM CFD, belonging to ANSYS. Figure 3 illustrates the proposed optimal mesh; it is a tetrahedral mesh with 302700 nodes, 18704 quads and 293020 hexas.
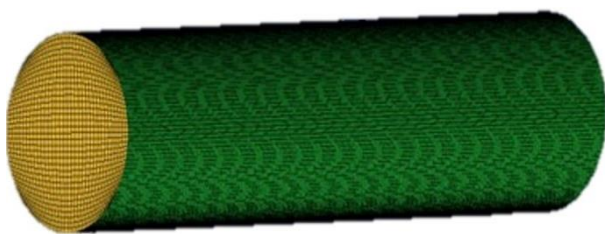

Figure 3 Optimal mallada of the geometry
Source: Own elaboration

Boundary conditions

The boundary conditions used in the simulations are: *pressure inlet* (at the duct inlet) with an inlet pressure variation of ±100 to ±500 mbar (±10000 and ±50000 Pa), *outlet vent* (duct outlet) and *wall* (for solid surfaces) which were implemented as a stationary wall and without slip conditions. These inlet conditions are taken for the study of velocities in the different cases. As can be seen in Figure 4, the geometry is divided into three walls *WALL_1* (located 0-100 mm along the tube), *WALL_2* (located 101-200 mm along the tube) and *WALL_3* (located 201-300 mm along the tube). However, the magnetic field will only be applied in the second section, referred to as *WALL_2*.
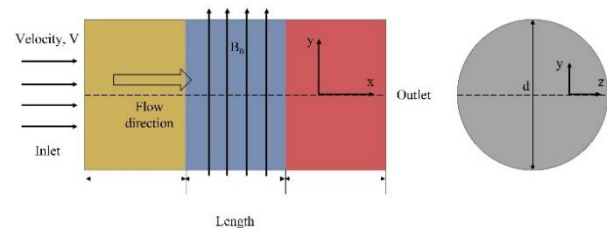
Figure 4 Boundary conditions
Source: Own elaboration

With these sections and once the velocity profiles are obtained, the boundary conditions for the implementation of the magnetic field are adjusted, which are: *velocity inlet* (at the duct inlet) where it is customized with the implementation of a UDF to define the velocity profile, *outlet vent* (duct outlet) and *wall* (for solid surfaces) which were implemented as stationary walls and without sliding conditions.

Considerations

The Herschel-Bulkley viscous model for the MR fluid is selected. Equation 1 representing this model is presented below:

$$\tau = \tau_0 + K(\gamma)^n \tag{1}$$

Where *K* indicates the consistency index (kg/ms), n the power law index, τ_0 the initial shear stress (Pa), γ the critical shear rate (1/s). However, to carry out the calculation of the initial shear stress, it is performed by Equation 2, this stress is calculated in relation to the applied magnetic field.

$$\tau_0(H) = C \cdot 2.717 \times 10^5 \cdot \Psi^{1.5239} \tanh(6.33 \times 10^{-6} H) \tag{2}$$

ORTEGA-ROMERO, Daysi Flor de Liz, ZÚÑIGA-CERROBLANCO, José Luis and HORTELANO-CAPETILLO, Juan Gregorio. Numerical analysis of the hydrodynamic behavior of a magnetoreological fluid. ECORFAN Journal-Taiwan. 2022

where τ_0 indicates the initial shear stress (Pa), C is a constant, Ψ is the volume fraction and H is the magnetic field strength (Teslas).

Governing equations

The equations of continuity of mass and momentum of steady motion of an incompressible MR fluid under a magnetic field in a cylindrical pipe are:

$$\nabla . V = 0 \qquad (3)$$

$$\rho \frac{DV}{Dt} = -\nabla P + \mu \Delta V + F_m \qquad (4)$$

where ∇P denotes the pressure gradient (Pa/m), ρ the fluid density (kg/m^3) and μ the dynamic viscosity of the fluid (kg/ms) and F_m is the electromagnetic force which can be expressed as follows:

$$F_m = \eta(J \times H) = J \times B \qquad (5)$$

Where J indicates the intensity of the electric current expressed below according to Ohm's law:

$$J = \sigma(E + V \times B) \qquad (6)$$

Where σ indicates the electrical conductivity of the fluid, E the magnitude of the electric field, V the average flow velocity vector and B is the magnetic field induction.

Results

However, these meshes present problems when converging and have high variations in the velocity results along the pipe, these variations are from 0.5 to 3 m/s, which indicates that these meshes are not optimal to use since the values are very variable and the results obtained will be very unreliable, these results are shown in Figure 2.

Having a deficient mesh, which does not comply with the necessary standards, can dramatically alter its characteristics and as a consequence have very unreliable results since they will not represent the expected phenomena.
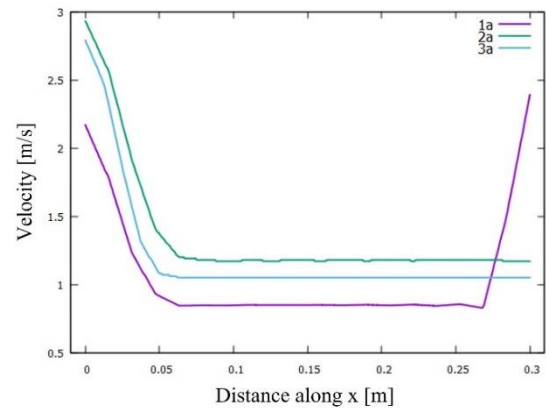
Graphic 2 Mesh convergence study for d=20mm, non-convergent
Source: Own elaboration

As can be clearly seen in Graph 3 and 4 for diameters of 20 and 30 mm, respectively, the smaller the size of the separation between the mesh nodes, i.e., the higher the mesh density, the higher the velocities, and after a certain mesh size, no significant change in velocities is observed. The information from the mesh convergence study for the pipe geometries is broken down in Table 2.
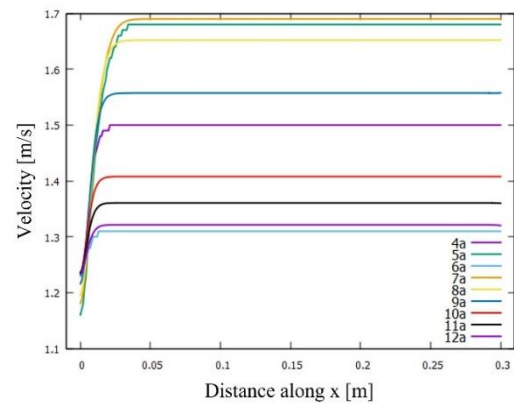

Graphic 3 Mesh convergence study for d=20mm, convergent
Source: Own elaboration
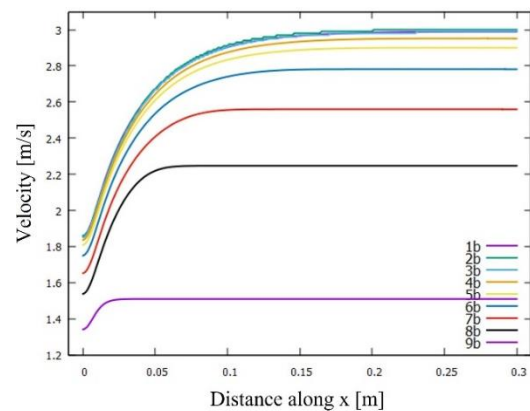
Figure 4 Mesh convergence study for d=30mm, convergent
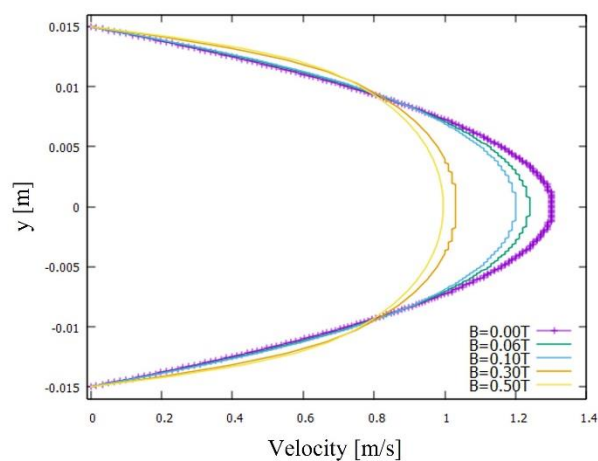*Source: Own elaboration*

The axial velocity profiles were plotted in Figure 5 with and without applied magnetic field. As can be clearly seen in the graph, the velocity value is 1.27 m/s for the situation when B = 0 Teslas, this for the Basonetic 5030 fluid in a 20 mm pipe, decreasing the velocity according to the increase of the magnetic field strength. As a result of these increases, flow velocity values of 1.16, 1.12, 1.02 and 0.983 m/s were found for magnetic field B = 0.06, 0.1, 0.3 and 0.5 Teslas, respectively.
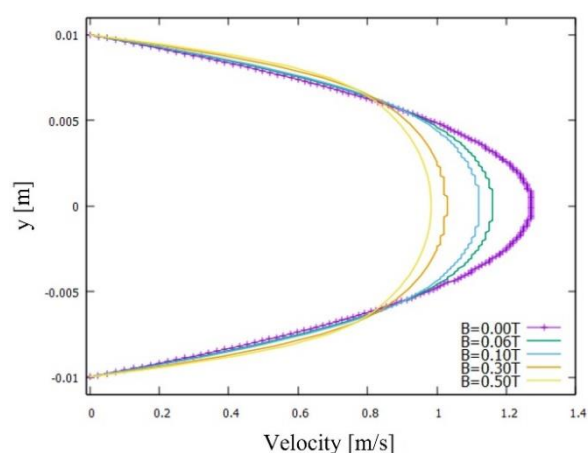
Graphic 5 Variations of velocity profiles as a function of increasing magnetic field, for d=20 mm, BASONETIC 5030
Source: Own elaboration

Similarly, these values turned out to be 1.23, 1.20, 1.03 and 0.995 m/s with the same increasing values of B for the pipe diameter of 30 mm while it was 1.30 m/s for the situation B = 0 Teslas as can be observed in Graphic 6.

Graphic 6 Variations of velocity profiles as a function of increasing magnetic field, for d=30 mm, BASONETIC 5030
Source: Own elaboration

The increase in magnetic field strength has caused the decrease in flow velocities for all MR fluids and the decrease in pipe diameter increases the flow velocity and pressure as expected.

In graphics7 and 8, the numerical velocity vectors of the pipe having 20 and 30 mm diameter for Basonetic 5030 fluid are shown, respectively. It is clear from the figure that the externally applied magnetic field in the *WALL_2* section has caused the velocity of the MR fluid flowing inside the pipe to decrease, since, when a magnetic field is applied, the particles tend to polarize and align with the field, decreasing the distance between molecules and, consequently, the resistance of the molecules to move increases. Thus, the viscosity of these fluids increases as a function of the intensity of the applied field.

When B = 0 Teslas the value of the velocity is equal to 1.27 m/s and the fluid flow results in smaller flow rates in situations B ≠ 0 Teslas compared to the situation where there is absence of magnetic field strength. At zero and low magnetic field values, the axial velocity profile is parabolic and as B increases, the profiles decrease maintaining the parabolic profile, as can be seen in Figure 5.
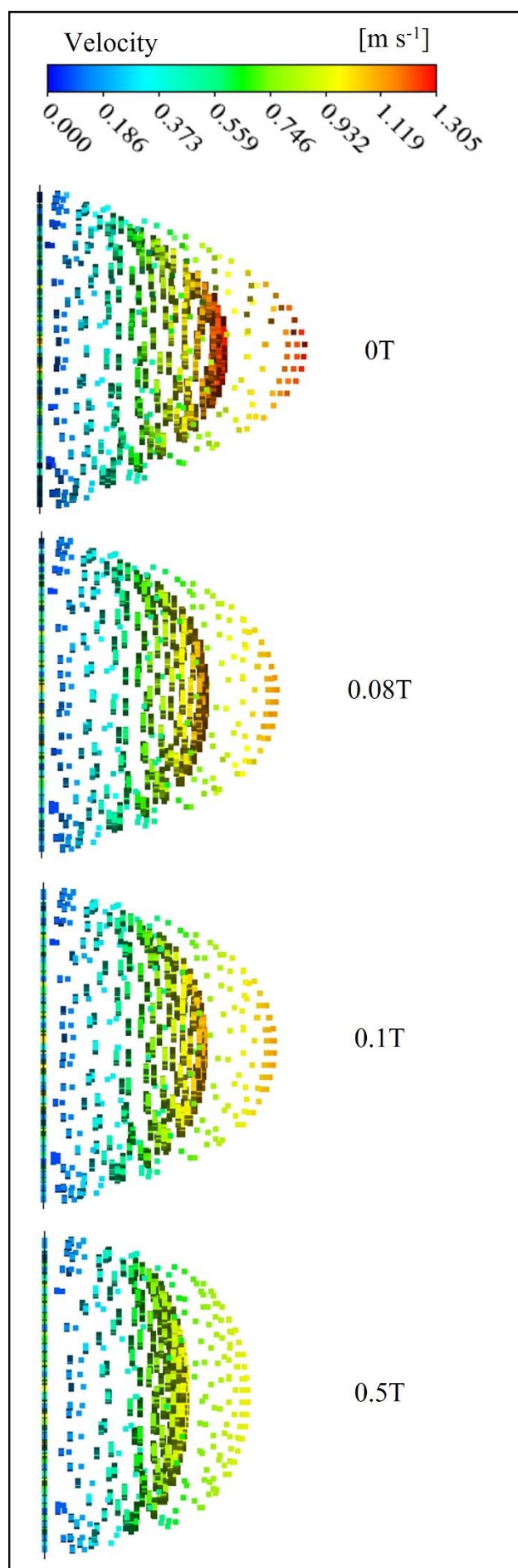
Graphic 7 Magnitude of velocity under different magnetic field strengths, d=20mm, BASONETIC 5030
Source: Own elaboration
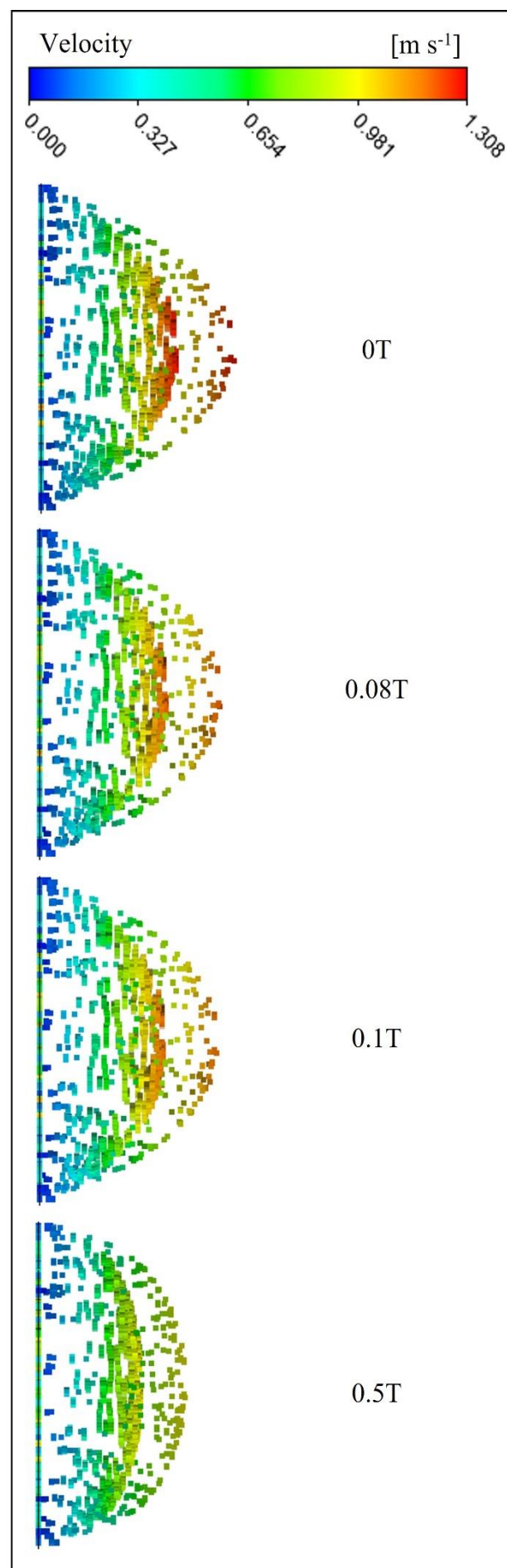
Graphic 8 Magnitude of velocity under different magnetic field strengths, d=30mm, BASONETIC 5030
Source: Own elaboration

This effect is obtained because when a particle is positioned perpendicularly in a uniform magnetic field, it begins to experience a force that will force it to change the direction of its velocity vector, causing it to move in a uniform circular motion.

The pressure differences measured in the numerical study and the velocity variations within the center of the pipe depend on the increase of the magnetic field strength.

In Graphic 9 it can be clearly seen, when the magnetic field increases, the pressure values increase. The pressure values obtained as 0.779 and 0.335 kPa in the situation of no applied magnetic field (B = 0 Teslas) for the fluid in the 20 and 30 mm pipes, respectively, have increased in the presence of the magnetic field and these values have gone to 2.720 and 1.588 kPa, respectively, for the value of the magnetic field B = 0.5 Teslas.
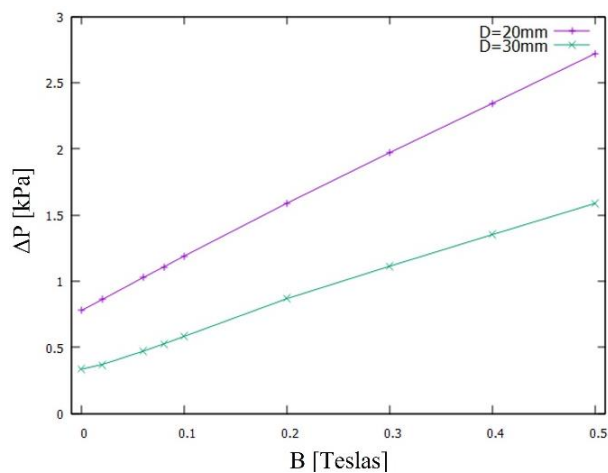
Graphic 9 Pressure variations as a function of increasing magnetic field strength
Source: Own elaboration

Conclusions

In this study, the laminar flow of a viscous and incompressible MR fluid was examined numerically. A CFD tool was used for the numerical study. The numerical study was performed using magnetic fields perpendicular to the flow of B = 0, 0.02, 0.06, 0.08, 0.1, 0.2, 0.3, 0.4 and 0.5 Teslas.

The fluid flow under the influence of the pressure gradient $\partial P/\partial x$ is in the x direction. Analyses were performed and compared for two different MR fluid flow models, the first being Newtonian (no magnetic field) and non-Newtonian (under magnetic field).

In the simulations, axial velocity values of 1.27 and 1.30 m/s have been found for Basonetic 5030 fluid for 20 and 30 mm pipe, respectively, when B = 0 Teslas.

It has been observed that the velocities and flow rates have increased with the decrease of the pipe diameter, considering that it is an incompressible fluid with stationary flow, the velocity in a conduit is inversely proportional to the surface area, since when the fluid is introduced in a region with smaller diameter, being smaller area, the velocity should be higher, but according to Bernoulli's equation, if the velocity increases, the pressure should decrease.

Regarding the results when the viscous model is adjusted, the increase of the magnetic field results in profiles with lower velocity, because as the magnetic field increases the fluid particles align in the direction of the field with higher velocity and consequently directly affects the viscosity of the fluid since the distance between the particles is smaller and therefore the resistance to flow is greater, due to the increase of this resistance as a function of the magnetic field, the pressure is affected; That is to say, the pressure increases with respect to the increase of the intensity of the magnetic field, since the smaller the distance between the particles, the more force is needed to move them. However, it is shown that the effect of the magnetic field is present in the simulation with the expected behavior.

It should be noted that the CFD simulation described in this work may represent a useful starting point to investigate more complex problems, such as non-stationary flows, more complex geometries or boundary conditions where slip is taken into account.

Nomenclature

ρ	Density (g/cm^3)
μ	Viscosity (Pa•s)
τ	Shear stress (Pa)
$\dot{\gamma}$	Critical shear rate (1/s)
σ	Electrical conductivity (µmho/cm)
ΔP	Pressure difference (Pa)
H	Magnetic field strength (Tesla)
d	Diameter (mm)
E	Magnitude of the electric field (V/m)
F_m	Electromagnetic force (Tesla)
J	Electrical current intensity (Amperio)
k	Consistency index (kg/m•s)
MR	Magnetorheological
N	Pressure gradient (Pa/m)
n	Energy law index
P	Pressure (Pa)
V	Velocity (m/s)
x	Axial coordinate
y	Radial coordinate
z	Tangential coordinate

References

Ata, WG, Oyadiji, S. (2014). An investigation into the effect of suspension configurations on the performance of tracked vehicles traversing bump terrains. *Vehicle System Dynamics*, *52 (7)*, 969–991. https://doi.org/10.1080/00423114.2014.909943

Bai, X-X, Chen, P, Qian, L.-J. (2015). Principle and validation of modified hysteretic models for magnetorheological dampers. *Smart Materials and Structures*, *24 (8)*, 085014. https://doi.org/10.1088/0964-1726/24/8/085014

Bai, X-X, Hu, W, Wereley, N. (2013). Magnetorheological Damper Utilizing an Inner Bypass for Ground Vehicle Suspensions. *IEEE Transactions on Magnetics*, *49 (7)*, 3422–3425. https://doi.org/10.1109/TMAG.2013.2241402

Boada, MJ, Calvo, JA, Boada, BL, et, A. (2011). Modeling of a magnetorheological damper by recursive lazy learning. *International Journal of Non-Linear Mechanics*, *46 (3)*, 479–485. https://doi.org/10.1016/j.ijnonlinmec.2008.11.019

Case, D, Taheri, B, Richer, E. (2014). Dynamical Modeling and Experimental Study of a Small-Scale Magnetorheological Damper. *IEEE/ASME Transactions on Mechatronics*, *19 (3)*, 1015–1024. https://doi.org/10.1109/TMECH.2013.2265701

Çeşmeci, Ş., & Engin, T. (2010). Modeling and testing of a field-controllable magnetorheological fluid damper. *International Journal of Mechanical Sciences*, *52*, 1036–1046. https://doi.org/10.1016/j.ijmecsci.2010.04.007

Chae, HD, Choi, S.-B. (2015). A new vibration isolation bed stage with magnetorheological dampers for ambulance vehicles. *Smart Materials and Structures*, *24 (1)*, 017001. https://doi.org/10.1088/0964-1726/24/1/017001

Deng, L, Sun, S, Christie, MD, et, A. (2019). Experimental testing and modelling of a rotary variable stiffness and damping shock absorber using magnetorheological technology. *Journal of Intelligent Material Systems and Structures*, *30 (10)*, 1453–1465. https://doi.org/10.1177/1045389X19835955

Ding, Y, Zhang, L, Zhu, H-T, et, A. (2013). A new magnetorheological damper for seismic control. *Smart Materials and Structures, 22 (11)*, 115003. https://doi.org/10.1088/0964-1726/22/11/115003

Gedik, E. (2017). Experimental investigation of magnetohydrodynamic flow in cıcrcular pipes and numerical analysis wıth computational fluid dynamics. *Journal of Applied Fluid Mechanics*, *10*, 801–811. https://doi.org/10.18869/acadpub.jafm.73.240.26830

Goldasz J, S. B. (2012). Nondimensional characterization of flow-mode magnetorheological/electrorheological fluid dampers. *Journal of Intelligent Material Systems and Structures*, *23*, 1545–1562.

Gurubasavaraju, M, Kumar, H, Mahalingam, A. (2018). An approach for characterizing twin-tube shear-mode magnetorheological damper through coupled FE and CFD analysis. *Journal of the Brazilian Society of Mechanical Sciences and Engineering*, *40 (3)*, 1–14. https://doi.org/10.1007/S40430-018-1066-Z

Huang, H, Sun, S, Chen, S, et, A. (2019). Numerical and experimental studies on a new variable stiffness and damping magnetorheological fluid damper. *Journal of Intelligent Material Systems and Structures, 30 (11)*, 1639–1652. https://doi.org/10.1177/1045389X19844003

Kim, H-C, Shin, Y-J, You, W, et, A. (2016). A ride quality evaluation of a semi-active railway vehicle suspension system with MR damper: Railway field tests. Proceedings of the Institution of Mechanical Engineers, Part F. *Journal of Rail and Rapid Transit*, *231 (3)*, 306–316.
https://doi.org/10.1177/0954409716629706

Liao, D. H. W. and W. H. (2011). Magnetorheological Fluid Dampers: A Review of Parametric Modelling. *Smart Materials and Structures*, *20*, 01–34.
https://doi.org/10.1088/0964-1726/20/2/023001

Omidbeygi F, H. S. (2012). Experimental study and CFD simulation of rotational eccentric cylinder in a magnetorheological fluid. *Journal of Magnetism and Magnetic Materials*, *324*, 2062–2069.
https://doi.org/10.1016/j.jmmm.2012.02.016

Pappas, Y., & Klingenberg, D. J. (2006). Simulations of magnetorheological suspensions in Poiseuille flow. *Rheologica Acta*, *45*, 621–629.
https://doi.org/https://doi.org/10.1007/s00397-005-0016-8

Phule, P. P. (2001). Magnetorheological (MR) fluids: principles and applications. *Smart Materials Bulletin*, *2001*(Elsevier), 7–10.

Qiang, F, Wang, D-H, Lei, X, et, A. (2017). A magnetorheological damper-based prosthetic knee (MRPK) and sliding mode tracking control method for an MRPK-based lower limb prosthesis. *Smart Materials and Structures*, *26 (4)*, 045030. https://doi.org/10.1088/1361-665X/aa61f1

Susan-Resiga, D., Bica, D., & Vékás, L. (2010). Flow behaviour of extremely bidisperse magnetizable fluids. *Journal of Magnetism and Magnetic Materials*, *322*, 3166–3172.
https://doi.org/10.1016/j.jmmm.2010.05.055

Wang, X., & Gordaninejad, F. (2006). Study of magnetorheological fluids at high shear rates. *Rheologica Acta*, *45*, 899–908.
https://doi.org/https://doi.org/10.1007/s00397-005-0058-y

Wu, B. (2010). CFD simulation of gas and non-Newtonian fluid two-phase flow in anaerobic digesters. *Water Research*, *44 (13)*, 3861–3874.
https://doi.org/10.1016/j.watres.2010.04.043

Yang, G. (2002). *Large-scale magnetorheological fluid damper for vibration mitigation: modeling, testing and control.* http://sstl.cee.illinois.edu/papers/gyang2_thesis.pdf

Automatic blood vessel detection using fractional Hessian matrices

Detección automática de vasos sanguíneos usando matrices Hessianas fraccionarias

MARTÍNEZ-JIMÉNEZ, Leonardo†*, LÓPEZ-LARA, Pedro, FLORES-BALDERAS, Adán and LÓPEZ-HERNÁNDEZ, Juan Manuel

Universidad de Guanajuato, Departamento de Estudios Multidisciplinarios, División de Ingenierías, Campus Irapuato-Salamanca, Av. Universidad S/N, Col. Yacatitas Yuriria Gto., , C.P. 38940. México.

ID 1st Author: *Leonardo, Martínez-Jiménez* / **ORC ID:** 0000-0002-7062-7154, **CVU CONACYT ID:** 165253

ID 1st Co-author: *Pedro, López-Lara* / **ORC ID:** 0000-0000-7908-3280

ID 2nd Co-author: *Adán, Flores-Balderas* / **ORC ID:** 0000-0002-1789-8393

ID 3rd Co-author: *Juan Manuel, López-Hernández* / **ORC ID:** 0000-0001-6546-4357

Abstract

The enhancement of blood vessels is a vital stage in imaging. The goal of this project is to improve the evaluation of the performance of a method for enhancing arteries in coronary angiograms, which use fractional derivatives. In this work an algorithm for automatic enhancement of vessels in coronary angiograms is evaluated, the method uses the Hessian matrix, the eigenvalues and the Grünwald-Letnikov fractional derivative with fractional order ω the in the interval $(1,3)$. The probes of the performance of the method were made using a set of 20 coronary angiograms with its respective ground-truth image and the area under the ROC's curve. The fractional orders are $2<\omega$ and the second interval $2\geq\omega$. The results show that the maximum values of area under the ROC's curve are obtained when the derivative order is in the interval $2<\omega<2.15$.

Evaluation, Coronary, Hessian matrix, Derivatives

Resumen

El realzado de vasos sanguíneos es una etapa vital en tareas de segmentación de imágenes médicas. El objetivo de este proyecto es mejorar la evaluación del desempeño de un algoritmo para realzado de arterias en angiogramas de coronarias que utiliza derivadas fraccionarias. En este trabajo se evalúa un método para realzado de vasos sanguíneos que utiliza la matriz Hessiana, los eigenvalores y la derivada Grünwald-Letnikov con ordenes fraccionarios ω en el intervalo $(1,3$. La evaluación del desempeño del realzador de angiogramas de orden fraccionario se realizó utilizando un conjunto de 20 imágenes de angiogramas de coronarias con su respectiva imagen ground-truth y el área bajo la curva ROC como parámetro de medición. Para las pruebas se usaron los intervalos de $2<\omega$ y $2\geq\omega$ de órdenes fraccionarios. Las pruebas muestran que se obtienen los mejores resultados cuando se utilizan ordenes de derivadas, $2<\omega<2.15$.

Evaluación, Coronarias, Matriz Hessiana, Derivadas

---

* Correspondence to Author (E-mail: leonardomj@ugto.mx)

† Researcher contributing as first author.

Introduction

The arteries are the most muscular, elastic vessels and carry blood from the heart to the arterioles. From here the blood enters the capillaries, the narrowest vessels, where all exchanges between blood and tissues take place, (Guzmán *et al.* 2022). That is why its correct operation is very important. An early diagnosis in arteries and the heart can help prevent irreversible damage, (Navarrete Chiriboga and Rivera Guerra 2022).

Enhance of vessels is a basic step in the segmentation process of medical images for Computer-Assisted Diagnosis (CAD). The target of the enhancement is improving the quality of the images to apply algorithms for diagnosis. To upgrade medical images like the angiograms, some algorithms have been proposed: some of them are based on morphological operations (Bouraoui *et al.* 2008), (Eiho and Qian 1997), (Lara *et al.* 2009), (Maglaveras *et al.* 2001). The others are based on the properties of the Hessian matrix (Kang *et al.* 2009) and (Frangi *et al.* 1998). In 2015 a segmentation method which works on two steps: first the structure of the vessels is detected using the properties of the Hessian matrix, after, an evolutive algorithm is utilized in thresholding tasks (Cruz-Aceves *et al.* 2015) and, in (Angeles Rojas, 2022) a method for detecting basal cell carcinoma using convolutional neural network and Support Vector Machine is described in (Angeles Rojas, 2022).

On the other hand, the Fractional Calculus (FC) is an extension of the traditional calculus and is devoted to integrals and derivatives of non-integer order. It is based on the properties of some special functions like the gamma function. Through the years, the FC has been transformed, and some different definitions of integrals and derivatives have been appeared. The first definitions were Riemann-Liouville integral and derivative, the Grünwald-Letnikov (GL) derivative (Capelas de Oliveira and Tenreiro Machado 2014), the Caputo fractional derivative (Caputo and Mainardi 1971), the Caputo-Fabrizio fractional derivative (Caputo *et al.* 2015), the Atangana-Baleanu definition (Atangana *et al.* 2016) and the Conformable derivative (Khalil *et al.* 2014), among others.

In the last years the FC has suffered a strong growth, due to practical applications in many knowledge fields. The first application was implemented by Abel solving the problem of the tautochrone curve (Abel 2012a), (Abel 2012b), since the number of applications has increased exponentially. Today the FC is utilized in fields like dynamic (Ahmad B. *et al.* 2015), viscoelastic models (Schiesselt *et al.* 1995) and (Meral *et al.* 2010), anomalous diffusion (Chen *et al.* 2010), electrical circuits (Ahmed *et al.* 2015) and (Guía *et al.* 2013), catenary based curves (Martinez-Jimenez *et al.* 2019), economic models (Baskonus *et al.* 2015), modelling of the movements of the electrons in conductive materials (Martinez-Jimenez L. *et al.* 2017) and (Karpinski *et al.* 2021), image processing (Amoako-Yirenkyi *et al.* 2016).

The mission of this work is refining the obtained results on (Martinez-Jimenez *et al.* 2018), using a more robust image base and comparing results with fractional orders in the interval $1.0 < \omega < 3.0$. The used base of images is composed by 20 coronary angiograms of 300×300 pixels, each image has a corresponding ground-truth image, which were generated by a specialist of the Instituto Mexicano del Seguro Social UMAE T1 León, (Cervantes-Sanchez *et al*. 2019).

The conformation of this work is as follows: in the next section the Hessian matrix and the GL fractional derivative are described, also, the Hessian matrix based method of Frangi is described. Following, the proposed method with the GL fractional derivatives to enhance angiograms is presented, after the results are evaluated using the ROC´s curves and they are displayed. Finally. some conclusions about the results are presented.

Theoretical foundations

Definition 1. Hessian Matrix $\mathbf{2 \times 2}$. Let $f = f(x, y)$ a continuous function defined in $\mathbb{R}^2$, then, the Hessian matrix of f denoted by $\mathcal{H}f(x, y)$, is defined as a 2×2 matrix which groups all the second order derivatives of $f(x, y)$:

$$\mathcal{H}f(x,y) = \begin{bmatrix} \frac{\partial^2 f}{\partial x^2} & \frac{\partial^2 f}{\partial x \partial y} \\ \frac{\partial^2 f}{\partial y \partial x} & \frac{\partial^2 f}{\partial y^2} \end{bmatrix}. \tag{1}$$

The method of Frangi works obtaining a vesselness measure of an image, the vesselness is the classification of each bit as a part of a vessel or not. This is achieved using the eigenvalues of the Hessian matrix of the image $\mathcal{H}I(x,y)$, and is defined by:

$$\mathcal{H}I = \begin{bmatrix} I_{xx} & I_{xy} \\ I_{yx} & I_{yy} \end{bmatrix}. \tag{2}$$

Where I_{xx}, I_{xy}, I_{yx} and I_{yy} denote the second order derivatives of the intensity image $I(x,y)$:

$$I_{xx} = \frac{\partial^2 I}{\partial x^2} = I(x,y) * \sigma^2 G_{xx}$$
$$I_{yy} = \frac{\partial^2 I}{\partial y^2} = I(x,y) * \sigma^2 G_{yy}$$
$$I_{xy} = \frac{\partial^2 I}{\partial x \partial y} = I(x,y) * \sigma^2 G_{xy}$$
$$I_{yx} = I_{xy}. \tag{3}$$

The symbol * indicates convolution, in addition, G_{xx}, G_{xy} and G_{yy} represent the second order of the Gaussian function $G(x,y)$ defined by:

$$G(x,Y) = \frac{1}{2\pi\sigma^2} \exp\left(-\frac{x^2+y^2}{2\sigma^2}\right), \tag{4}$$

Since $\mathcal{H}I$ is a symmetrical matrix the eigenvalues λ_1 and λ_2 are given by:

$$\alpha = \sqrt{(I_{xx} - I_{yy})^2 + 4I_{xy}}$$
$$\lambda_1 = \frac{I_{xx}+I_{yy}+\alpha}{2}$$
$$\lambda_2 = \frac{I_{xx}+I_{yy}-\alpha}{2}, \tag{5}$$

with the eigenvalues λ_1 and λ_2 the vesselness measure is calculated with the expression:

$$V_F = \begin{cases} \exp\left(-\frac{R_\beta^2}{2\beta^2}\right)\left[1 - \exp\left(-\frac{s^2}{2\gamma^2}\right)\right], & if\ \lambda_1,\lambda_2 > 0 \\ 0 & ,Otherwise \end{cases} \tag{6}$$

$R_\beta = \lambda_1/\lambda_2$, $s = \sqrt{\lambda_1 + \lambda_2}$, $\beta = 0.5$, and γ is defined as a half of the maximum value of s, the final vesselness image is obtained using different scales for σ for each pixel of the image $I(x,y)$.

Grünwald-Letnikov Fractional derivative

First to all, consider the ratio which define the derivative of a $f(x)$ function

$$f_r'(x) = \lim_{\Delta x \to 0} \frac{f(x+\Delta x)-f(x)}{\Delta x}$$
$$f_d'(x) = \lim_{\Delta x \to 0} \frac{f(x)-f(x-\Delta x)}{\Delta x}, \tag{7}$$

The expressions $f_r'(x)$ and $f_d'(x)$ are defined as the forward and backward derivatives. Then, the same process is applied again:

$$f_{d(x)}'' = \lim_{\Delta x \to 0} \frac{\left[\lim_{\Delta x \to 0} \frac{f(x)-f(x-\Delta x)}{\Delta x}\right] - \left[\lim_{\Delta x \to 0} \frac{f(x-\Delta x)-f(x-2\Delta x)}{\Delta x}\right]}{\Delta x} \tag{8}$$

simplifying we have:

$$f_{d(x)}'' = \lim_{\Delta x \to 0} \frac{f(x)-2f(x-\Delta x)+f(x-2\Delta x)}{\Delta^2 x} \tag{9}$$

to find the third order derivative the procedure similar:

$$f_{d(x)}''' = \lim_{\Delta x \to 0} \frac{1}{\Delta^3 x}\left[f(x) - 3f(x - \Delta x) + 3f(x - 2\Delta x) - f(x - 3\Delta x)\right] \tag{10}$$

since the behavior of the coefficients is binomial, it is easy to find the n-order derivative using the binomial formula:

$$f_d^{(n)}(x) = \lim_{\Delta x \to 0} \frac{1}{\Delta^n x} \sum_{n=0}^{n}(-1)^k \binom{n}{k} f(x - k\Delta x) \tag{11}$$

where $n \in \mathbb{Z}_+$, and the binomial coefficient is given by:

$$\binom{n}{k} = \frac{n!}{k!(n-k)!}, \tag{12}$$

if, n is substituted by an arbitrary value $\alpha \epsilon \mathbb{R}$, the binomial coefficient is defined by:

$$\binom{\alpha}{k} = \frac{\Gamma(\alpha+1)}{k!\Gamma(\alpha+1-k)}. \tag{13}$$

$\Gamma(\cdot)$ is the gamma function which extends the definition of factorial to arbitrary values.

Definition 2: Grünwald-Letnikov fractional derivative. The fractional forward GL derivative is defined as:

$$f_d^{(\alpha)}(x) = \lim_{\Delta x \to 0} \frac{1}{\Delta^\alpha x} \sum_{k=0}^{\infty}(-1)^k \binom{\alpha}{k} f(x - k\Delta x) \tag{14}$$

and, the fractional backward GL derivative of $f(x)$ is defined as:

and the backward GL is:

$$f_r^{(\alpha)}(x) = \lim_{\Delta x \to 0} \frac{1}{\Delta^\alpha x} \sum_{k=0}^{\infty}(-1)^k \binom{\alpha}{k} f(x + k\Delta x) \tag{15}$$

In the case when $\Delta x = 1$ a simplest version of (14) is obtained

$$D^{(\alpha)}(x) = f(x) - \alpha f(x-1) + \frac{\Gamma(\alpha+1)}{2\Gamma(\alpha-1)} f(x-2) - \frac{\Gamma(\alpha+1)}{3!\Gamma(\alpha-2)} f(x-3) + \cdots. \qquad (16)$$

Even though the GL is an old definition, it is very useful in discrete applications, like the image processing, due to its practicality to be implemented in computer systems.

Enhancing blood vessel using fractional Hessians

In order to apply the fractional derivatives to the algorithm of Frangi a new definition based on Hessian matrixes is necessary.

Definition 3. Fractional Hessian matrixes 2×2 ***of order*** $1 + \varphi$***, and*** $2 + \varphi$***.*** The fractional Hessian matrix 2×2 of the order and $1 + \varphi$, where $\varphi \in (0,1]$ is defined as:

$$\mathcal{H}^{1+\varphi} I = \begin{bmatrix} \frac{\partial^{1+\varphi} I}{\partial x^{1+\varphi}} & \frac{\partial^{1+\varphi} I}{\partial x^{\varphi} \partial y} \\ \frac{\partial^{1+\varphi} I}{\partial y \partial x^{\varphi}} & \frac{\partial^{1+\varphi} I}{\partial y^{1+\varphi}} \end{bmatrix} \qquad (17)$$

and the fractional Hessian matrix 2×2 of order $2 \leq 1 + \varphi < 3$, is defined as follows:

$$\mathcal{H}^{2+\varphi} I = \begin{bmatrix} \frac{\partial^{2+\varphi} I}{\partial x^{2+\varphi}} & \frac{\partial^{2+\varphi} I}{\partial x^{1+\varphi} \partial y} \\ \frac{\partial^{2+\varphi} I}{\partial y \partial x^{1+\varphi}} & \frac{\partial^{2+\varphi} I}{\partial y^{2+\varphi}} \end{bmatrix} \qquad (18)$$

The proposed method in (Martinez-Jimenez, L. *et Al.* 2018), works using the GL fractional derivative to modifies the Frangi's algorithm creating a fractional Hessian matrix $\mathcal{H}^{\omega} I$, with $2 \leq \omega < 3$. The algorithm was probed using an angiogram set of 4 images with its respective ground-truth image, and the area under the ROC's curve. Despite was no probed, was mentioned that the performance of the algorithm decayed when $\omega < 2$.

In the present project a similar methodology to (Martinez-Jimenez *et al.* 2018) is implemented, using the GL fractional derivative and the ROC´s curve. However, here, a set of 20 angiograms with its respective ground-truth images were utilized. The order of the fractional derivatives was φ, $2 \leq \omega < 3$. Then, the eigenvalues were calculated and with them the vesselness images for each pixel.
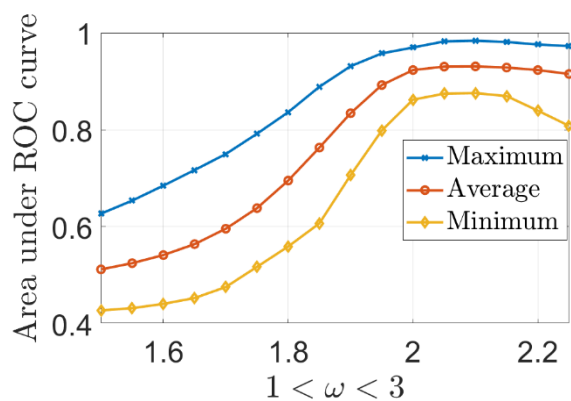
Results

The ROC (*Receiver Operating Characteristic*) is a powerful tool, used to evaluate the performance of a binary classifier. In this case is about the classification the pixels as vessel or not, the results are in the four situations:

- **TP** True positive: A vessel pixel was correctly classified, as a vessel pixel.

- **TN** True Negative: A no vessel pixel was correctly classified as a no vessel pixel.

- **FP** False Positive: A no vessel pixel was incorrectly classified as vessel pixel.

- **FN** False Negative: A vessel pixel was incorrectly classified as no vessel pixel.

The area under the ROC's curve is a graphically way to represent the ratio between the TP against the FP and, the shape of the curve tends to be a rectangle when the total of the TP is near to 100%.

In order to analyze the behavior of the proposed algorithm with fractional orders the study was performed into two steps: in the first one, the algorithm was evaluated using the fractional order in the interval $1 < \omega \leq 2$, and in the second the interval was $2 < \omega < 3$. Each angiogram image was analyzed using the area under the ROC´s curve and each fractional value. With the set of results the mean, the maximum and the minimum for each value of ω was calculated. The results are shown in the Plot 1.

Plot 2 shows, the result to apply the algorithm to the angiogram 13, and the fractional orders: $\omega = 1.95$, $\omega = 2$, and some values $\omega > 2$. We can see that the value of the area is smaller when $\omega < 0$ than when $\omega = 0$ and increases as $\omega > 0$, however, it reaches its maximum approximately at $\omega = 2.9$, after it is decreasing. Specially for $\omega > 2.13$.

MARTÍNEZ-JIMÉNEZ, Leonardo, LÓPEZ-LARA, Pedro, FLORES-BALDERAS, Adán and LÓPEZ-HERNÁNDEZ, Juan Manuel. Automatic blood vessel detection using fractional Hessian matrices. ECORFAN Journal-Taiwan. 2022

Graphic 1 Average, maximum, and minimum values obtained of the set of angiograms and the ROCS's curve, each image was evaluated with fractional orders $1 < \omega < 3$
Source: Own elaboration

The curves show that, using fractional orders $\omega < 2$, the area values are smaller than in the ordinary solution ($\omega = 2$), this, confirms that, to use fractional order $\omega < 2$, does not improve the results. However, using fractional orders $\omega > 2$, help to improve the area values, respect to the ordinary solution, the best results are found when $2.05 \leq \omega \leq 2.13$, but the area values decaying with $\omega > 2.13$.
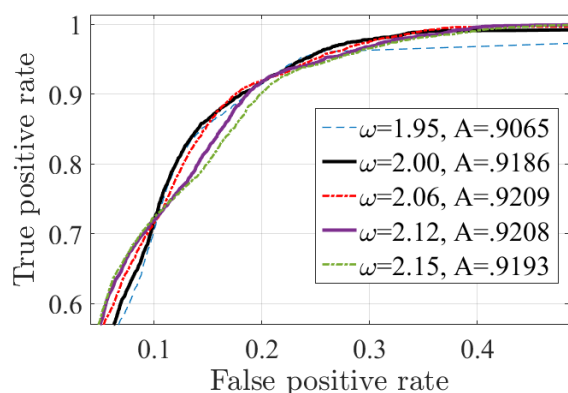

Graphic 2 ROC'S curves using some values of ω applied to the angiogram 13 of the set. A is the corresponding area under the curve value
Source: Own elaboration

In the Figure 1 the angiogram 13 and its corresponding ground-truth image are shown, in the ground-truth the arteries was marked by a specialist, is utilized as reference to evaluate the performance of the algorithm.
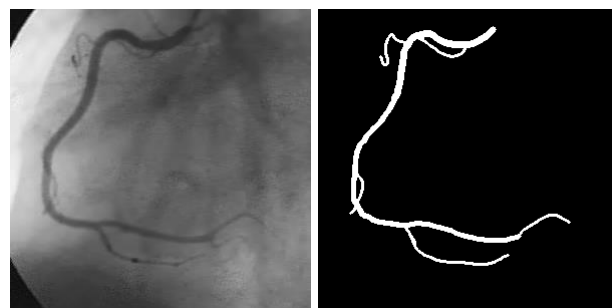

Figure 1 Angiogram 13 (a) original image and (b) ground-truth image
Source: Cervantes-Sanchez et al. 2019

In the Figure 2, the results of apply the algorithm to the angiogram 13 with the fractional orders $\omega = 1.95$, and $\omega = 2.0$ (traditional solution), we can see that, the result when $\omega = 1.95$ is worse that, the traditional one.
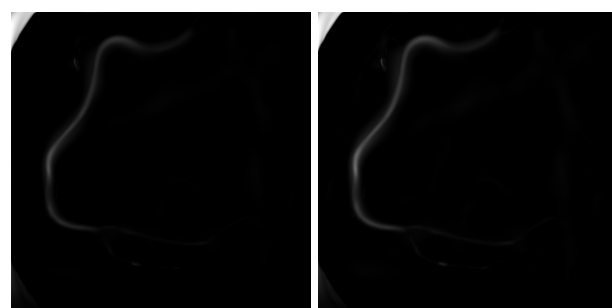
Figure 2 Obtained result using the algorithm in the angiogram 13, (a) with fractional order $\omega = 1.95$ and (b) with $\omega = 2.0$ (traditional solution)
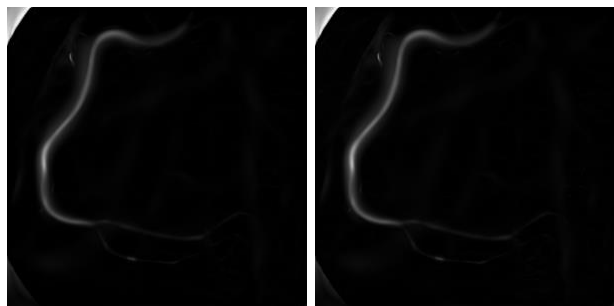*Source: Own elaboration*

In the Figure 3 the results are shown when the algorithm is applied using the fractional values $\omega > 2$, (a) with fractional order $\omega = 2.06$ and (b) with fractio0nal order $\omega = 2.09$, it was the best result.
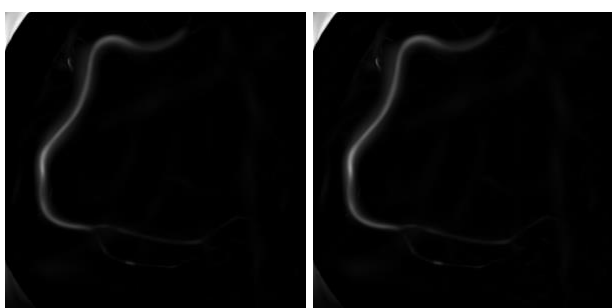
Figure 3 Obtained result using the algorithm in the angiogram 13, (a) with fractional order $\omega = 2.06$ and (b) with $\omega = 2.09$ the best result was obtained here
Source: Own elaboration

In the Figure 4 the results are shown when the algorithm is applied using the fractional values $\omega > 2$, (a) with fractional order $\omega = 2.12$ and (b) with fractio0nal order $\omega = 2.15$.

Figure 4 Obtained results using the algorithm in the angiogram 13, (a) with fractional order ω = 2.12 and (b) with ω = 2.15 the best result was obtained here
Source: Own elaboration

Attached

The angiograms database is available in: http://personal.cimat.mx:8181/~ivan.cruz/Databases.html

Acknowledgment

Conclusions

In this work the proposed algorithm in 2018 based on the Frangi's one and fractional derivatives, was evaluated using fractional orders $2 < \omega < 3$ and the area under the ROC's curve. The evaluation was using fractional orders in two steps, in the first, the order was in the interval $1 < \omega < 2$, and, in the second, was in the interval $2 < \omega < 3$. The evaluation of the development of the algorithm was made using 20 angiograms with its respective ground-truth and the ROC's curves. The results show that the best results are obtained when the derivative order is in the interval $2 < \omega < 2.15$.

References

Abel, N. (2012). Oeuvres complètes de Niels Henrik Abel: Nouvelle édition (Cambridge Library Collection - Mathematics) (L. Sylow & S. Lie, Eds.). Cambridge: Cambridge University Press. DOI: https://doi.org/10.1017/CBO9781139245807.

Abel, N. (2012). Oeuvres complètes de Niels Henrik Abel: Nouvelle édition (Cambridge Library Collection - Mathematics) (L. Sylow & S. Lie, Eds.). Cambridge: Cambridge University Press. DOI: https://doi.org/10.1017/CBO9781139245814.

Ahmad, B., Batarfi, H., Nieto, J. J., Otero-Zarraquiños, O., and Shammakh W. (2015). Projectile motion via Riemann-Liouville calculus, Advances in Difference Equations, 63. DOI: https://doi.org/10.1186/s13662-015-0400-3.

Ahmed, A., Nieto J. J., Venktesh, V. (2015). Fractional Electrical Circuits, Advances in Mechanical Engineering, 7(12) 1–7 DOI: https://doi.org/10.1177/1687814015618127.

Amoako-Yirenkyi P., Appati J. K., and Dontwi I. K. (2016). A new construction of a fractional derivative mask for image edge analysis based on Riemann-Liouville fractional derivative, Advances in Difference Equations, 2016 (238). DOI: https://doi.org/10.1186/s13662-016-0946-8.

Angeles Rojas, J. A. (2022). Detección de carcinoma basocelular utilizando red neuronal convolucional y Support Vector Machine. (Bachelor's thesis). Universidad Nacional Mayor de San Marcos. DOI: https://cybertesis.unmsm.edu.pe/handle/20.500.12672/18365.

Atangana A., and Baleanu, D. (2016). New fractional derivatives with nonlocal and non-singular kernel: theory and application to heat transfer model. Thermal Science, 20(2), 763-769. DOI: 10.2298/TSCI160111018A.

Baskonus, H. M., Mekkaoui T., Hammouch, Z., and Bulut, H. (2015). Active Control of a Chaotic Fractional Order Economic System, Entropy. 17, 5771-5783, DOI: 10.3390/e17085771. (Haci Mehmet Baskonus, Toufik Mekkaoui, Zakia Hammouch and Hasan Bulut. Active Control of a Chaotic Fractional Order Economic System, Entropy. 2015, 17, 5771-5783. DOI: https://doi.org/10.3390/e17085771.

Bouraoui, M., Ronse, C., Baruthio, J., Passat, N., and Germain, P. (2008). Fully Automatic 3D Segmentation of Coronary Arteries Based on Mathematical Morphology. Proc. 5th IEEE International Symposium on Biomedical Imaging (ISBI 2008): From Nano to Macro, IEEE, (May 2008), 1059–1062. DOI: 10.1109/ISBI.2008.4541182.

Capelas de Oliveira, E., and Tenreiro Machado, J., A. (2014). A review of definitions for fractional derivatives and integral. Mathematical Problems in Engineering, 2014, 1-6. DOI: https://doi.org/10.1155/2014/238459.

Caputo, M., and Fabrizio, M. (2015). A new Definition of Fractional Derivative without Singular Kernel, Progr. Fract. Differ. Appl. 1(2), 73-85. DOI: http://dx.doi.org/10.12785/pfda/010201.

Caputo, M., and Mainardi, F. (1971). A new dissipation model based on memory mechanism. Pure Appl. Geophys., 91, 134-147. DOI: https://doi.org/10.1007/BF00879562.

Cervantes-Sanchez, F., Cruz-Aceves, I., Hernandez-Aguirre, A., Hernandez-Gonzalez, M., A., and Solorio-Meza, S., E. (2019). Automatic Segmentation of Coronary Arteries in X-ray Angiograms using Multiscale Analysis and Artificial Neural Networks. Applied Sciences 9(24). 5507. DOI: https://doi.org/10.3390/app9245507.

Chen, W., Sun H., Zhanga, X., and Dean, K. (2010). Anomalous diffusion modeling by fractal and fractional derivatives. Computers & Mathematics with Applications, 59(5),1754-1758. DOI: https://doi.org/10.1016/j.camwa.2009.08.020.

Cruz-Aceves, I., and Hernandez-Aguirre A. (2015). Segmentation of Coronary Angiograms Using a Vesselness Measure and Evolutionary Thresholding: Design of Intelligent Systems Based on Fuzzy Logic, Neural Networks and Nature Inspired Optimization, 601. Series Studies in Computational Intelligence. 269-289. DOI:10.1007/978-3-319-17747-2_22.

Eiho S. and Qian Y. (1997). Detection of coronary artery tree using morphological operator. Computers in Cardiology. 24. 525–528. DOI: 10.1109/CIC.1997.647950

Frangi, A., Niessen. W., Vincken, A., and Viergever, M. (1998). Multiscale Vessel Enhancement Filtering. Proc. Medical Image Computing and Computer-Assisted Intervention (MICCAI 1998). 1496. Springer, 130-137. DOI: https://doi.org/10.1007/BFb0056195.

Guia, M., Gomez, F., and Rosales, J. (2013). Analysis on the time and frequency domain for the RC electric circuit of fractional order. Open Physics, 11(10), 1366-1371. DOI: https://doi.org/10.2478/s11534-013-0236-y.

Guzman, D., Roca, S., Pimienta, M., Estrella, C. (2022). Impacto del entrenamiento específico de fuerza muscular sobre los niveles de tensión arterial en adultos mayores con hipertensión arterial: Caso del geriátrico "Cabaña Mis nonos" Guaymallén Mendoza. (Bachelor's thesis). Universidad Juan Agustín Maza. DOI: http://repositorio.umaza.edu.ar/handle/00261/2913.

Kang, W., Wang, K., Chen, W., and Kang, W. (2009). Segmentation Method Based on Fusion Algorithm for Coronary Angiograms. Proc. 2nd International Congress on Image and Signal Processing (CISP 2009). (Oct. 2009), 1–4. DOI: 10.1109/CISP.2009.5303615.

Karpinski, K., Sylwia, Zielinska-Raczynska S., and Ziemkiewicz, D. (2021). Fractional Derivative Modification of Drude Model, Sensors. 21, 4974. DOI: https://doi.org/10.3390/s21154974.

Khalil, R., Al Horani, M., Yousef, A., and Sababheh A. (2014). A new definition of fractional derivative, Journal of Computational and Applied Mathematics, 264 (2014) 65–70. DOI: https://doi.org/10.1016/j.cam.2014.01.002.

Lara, D. S.D., Faria, A. W. C., Araujo, A. A., Menotti, D. (2009). A Semi-Automatic Method for Segmentation of the Coronary Artery Tree from Angiography, Proc. XXII Brazilian Symposium on Computer Graphics, and Image Processing (SIBGRAPI 2009), IEEE. (Oct. 2009), 194–201. DOI: 10.1109/SIBGRAPI.2009.41.

Maglaveras, N., Haris, K., Efstratiadis, S., Gourassas, J., and Louridas, G. (2001). Artery skeleton extraction using topographic and connected component labeling, Computers in Cardiology. 28, 17–20. DOI: 10.1109/ICIP.2001.958497.

Martinez-Jimenez, L., Cruz-Duarte, J. M., Rosales, J. J., and Cruz-Aceves I. (2018). Enhancement of Vessels in Coronary Angiograms Using a Hessian Matrix Based on Grunwald-Letnikov Fractional Derivative. In Proceedings of the 2018 8th International Conference on Biomedical Engineering and Technology (ICBET '18). Association for Computing Machinery, New York, NY, USA, 51–54. DOI: https://doi.org/10.1145/3208955.3208971.

Martinez-Jimenez, L., Cruz-Duarte, J. M., Rosales-Garcia, J. J. (2019). Fractional solution of the catenary curve, Math Meth Appl Sci. 1–10. DOI: https://doi.org/10.1002/mma.5608.

Martinez-Jimenez, L., Rosales-Garcia, J. J., Ortega-Contreras, A., and Baleanu, D. (2017). Analysis of Drude model using fractional derivatives without singular kernels, Open Phys. 15, 627–636. DOI: https://doi.org/10.1515/phys-2017-0073.

Meral, F. C., T.J., Royston T. J., and Magin R. (2010). Fractional calculus in viscoelasticity: An experimental study. Communications in Nonlinear Science and Numerical Simulation, 15(4), 939-945 DOI: https://doi.org/10.1016/j.cnsns.2009.05.004.

Navarrete Chiriboga, B. A., and Rivera Guerra, L. M. (2022). Tamizaje cardiológico neonatal por oximetría de pulso como método para la detección temprana de cardiopatías congénitas en el Hospital General Guasmo Sur, servicio de neonatología en el año 2021. (Bachelor's thesis). Universidad Católica de Santiago de Guayaquil. DOI: http://repositorio.ucsg.edu.ec/handle/3317/18946.

Schiesselt, H., Metzlert, R., Blument, A. and Nonnemacher T. F. (1995). Generalized viscoelastic models: their fractional equations with solutions. Journal of Physics A: Mathematical and General, Gen. 28 6567, 6567-4584. DOI: https://doi.org/10.1088/0305-4470/28/23/012.

Use of unstructured meshes for wave height and particles horizontal displacement analysis in central zone Veracruz, Mexico

Utilización de mallas no estructuradas para el análisis de altura de ola y desplazamiento horizontal de partículas en la zona central de Veracruz, México

AGUILERA-MENDEZ, José María†*, JUAREZ-TOLEDO, Carlos, MARTINEZ-CARRILLO, Irma and VERA-POPOCA, Roberto Ismael

Universidad Autónoma del Estado de México, Unidad Académica Profesional Tianguistenco.

ID 1st Author: *José María, Aguilera-Méndez* / **ORC ID:** 0000-0002-9826-421X, **CVU CONACYT ID:** 66670

ID 1st Coauthor: *Carlos, Juárez-Toledo* / **ORC ID:** 0000-0002-7440-3246, **Researcher ID Thomson:** C-1368-2016, **CVU CONACYT ID:** 39912

ID 2nd Co-author: *Irma, Martínez-Carrillo* / **ORC ID:** 0000-0002-7952-4418, **Researcher ID Thomson:** B-9264-2016, **CVU CONACYT ID:** 39914

ID 3rd Co-author: *Roberto Ismael, Vera-Popoca* / **ORC ID:** 0000-0003-2574-122X, **CVU CONACYT ID:** 1041051

Abstract

The objective research is the calculation of free-floating particle displacement trajectory using the Simulating Waves Nearshore (SWAN) software having as base unstructured meshes to get the diagram of the study area. Third-party tools and data were used, such as bathymetry, wave and tide data from the Global Ensemble Forecast System-Wave (GEFS-Wave) and data processing using SWAN. The modelling software and some local developments were used to generate valid Delaunay diagrams for the central zone of the Veracruz state, Mexico. For the configuration of the experiments, we worked with physics variables of the modelling software until achieving one that resembled the real conditions of the area; once the similarity was achieved, it was possible to run the experiments to obtain the wave height and frequency and replace the values in the horizontal displacement equation until obtaining the spaghetti diagrams that indicate the possible paths of the particles.

Resumen

El objetivo de la investigación es el cálculo de la trayectoria de desplazamiento de partículas de libre flotación utilizando el software Simulating Waves Nearshore (SWAN) teniendo como base mallas no estructuradas para obtener el diagrama del área de estudio. Se utilizaron herramientas y datos de terceros, como lo fueron la batimetría, datos de olas y mareas del Global Ensemble Forecast System-Wave (GEFS-Wave) y el procesamiento de los datos utilizando SWAN. El software de modelación y algunos desarrollos locales fueron utilizados para generar los diagramas de Delaunay válidos para la zona central del estado de Veracruz, México. Para la configuración de los experimentos se trabajó con variables de física del software de modelación hasta lograr una que asemejara las condiciones reales de la zona; una vez que se logró la similitud, fue posible ejecutar los experimentos para la obtención de altura y frecuencia de la ola y reemplazar los valores en la ecuación de desplazamiento horizontal hasta obtener los diagramas de espagueti que indican las posibles rutas de las partículas.

Wave height, Particles displacement, unstructured mesh

Altura de ola, Movimiento partículas, Mallas no estructuradas

---

---

* Correspondence to Author (E-mail: jaguileram001@alumno.uaemex.mx)
† Researcher contributing as first author.

Introduction

The study that was developed bases its postulates on the theory of waves and their formation. It would be impossible to understand the wave's height without considering the action exerted by the wind on the sea. This study does not consider the height of the waves generated by extraordinary phenomena such as hurricanes and earthquakes; whose generation and propagation consider different formulas in addition to values of variables such as salinity, density, seabed, etc. and that due to their propagation speed, they are more complicated to predict (Musinguzi et al., 2019).

A wave is considered to be the sinusoidal variation in elevation of the sea surface and can be defined as a height, **H**, which is the vertical distance from the crest to the trough of the wave in feet or meters, with wavelength, **λ**, which is the distance in feet or meters between two similar points on the wave and the wave period, **T**, which is the time in seconds or minutes it takes for the wave to repeat itself.

From **Figure 1**, several additional variables are obtained that helps to represent the wave movement, among them:

Wave frequency, $\omega = 2\pi/T$

Wave number, $k = 2\pi/\lambda$
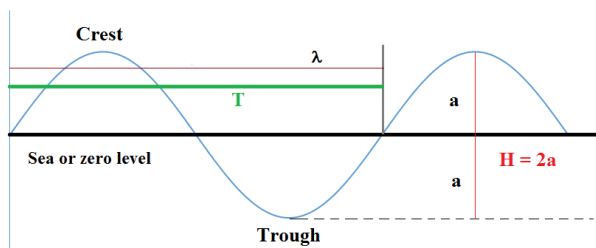
Figure 1 Wave parts and measurements identification
Source: Own elaboration

A wave on the ocean surface is considered to be the result of the combination of different disturbing and restoring forces that are in dynamic equilibrium. Consequently, the tides could be considered as waves of very long period. It is considered that a wave generated by the force of gravity has a period of between 1 and 30 seconds in duration; and the tides have a period of between 12 - 24 hours (Pecher & Kofoed, 2017).

The waves always start as small waves that increase in size due to the constant supply of energy provided by the wind. As long as the wind continues to blow, the waves reach their limit, beyond which they do not grow due to the balance caused by the loss of energy. This loss of energy should not be understood as the sea entering a static moment since when the wind stops blowing, the waves will continue to exist with the ability to travel great distances while conserving practically the same amount of energy (Friedman & Tillich, 2004; Ringler et al., 2013). In this study, we will separate the waves into two groups: wind waves created by local winds and tidal waves, created by winds that do not blow in the area. Although, all waves are both created by the effect of the previous wind and are affected by the local wind; it is the local wind that generates waves that are out of the ordinary. Although the separation of the waves generated by local winds and swell waves is a way that facilitates the description of the conditions in a particular point of the ocean and, until now, it must be considered one of the main pieces when carrying out trajectory forecasts of free-floating objects on the surface of the oceans (Johns et al., 2020).

The elevation of the water surface ζ is understood to be given by the following equation:

$$\zeta = \frac{H}{2} \cos\left[2\pi\left(\frac{x}{\lambda} - \frac{t}{T}\right)\right] \tag{1}$$

This change in ocean surface elevation is the result of an elliptical motion of water particles, which extends below the surface; and the amplitude of the motion decreases exponentially with depth. So it is obtained that for the vertical displacement of the water particles ζ**(z)** is given by the formula, where **d** depends on the depth of the seabed. That measure generally is taken from bathymetry

$$\zeta(z) = \frac{H}{2} \cos\left[2\pi\left(\frac{x}{\lambda} - \frac{t}{T}\right)\right] \frac{sinh[2\pi(z+d)/\lambda]}{sinh[2\pi d\lambda]} \tag{2}$$

And the horizontal displacement ξ**(z)**:

$$\xi(z) = \frac{H}{2} \sin\left[2\pi\left(\frac{x}{\lambda} - \frac{t}{T}\right)\right] \frac{cosh[2\pi(z+d)/\lambda]}{sinh[2\pi d\lambda]} \tag{3}$$

Once the equations to determine the movement of the particles are available, it is important to have the bathymetry of the area and generate its mesh to run the corresponding simulations. For our analysis, we will work with an unstructured mesh based on Delaunay triangles; that in areas where there are sudden changes in depth as the seashore, as well as intense meteorological changes, analyzes with unstructured meshes have been more accurate than analyzes with structured meshes (Aguilera-Méndez, Juárez-Toledo, Martínez-Carrillo, & Vera-Popoca, 2021; Weatherill, 1992). Together with the bathymetry, the friction factor with the seabed should be considered; JONSWAP is widely used but RIPPLES will be used in the experiment since it has shown that in this coordinates with the spaces close to the coast its results on the wave cycle in unusual conditions are more accurate.

Although the experiment seeks to obtain the waves total height on the beach, the effect that the lunar cycles have on the tide must be considered; This is because the simulation software performs the calculations for the waves height caused by the wind and does not contemplate a dynamic generation of the tide with the lunar cycles, so it must be entered manually. There are some oceanographic models from which the initial tidal data is taken. For this experiment we will use the data set of the Global Ensemble Forecast System-Wave (GEFS-Wave) (Toth & Kalnay, 1997), which is an assemble of the GFS and WW3 models administrated by National Oceanic and Atmospheric Administration (NOAA); This model has the peculiarity that 1) the data is verified and 2) it takes the 6 hours of the last forecast generated in order to obtain continuity of the forecasts and discard the 00 or start time.

By definition the forecasts wave heights are the "Significant Wave Height"; this is the average wave height (trough to crest) of the highest 1/3 of the forecast waves. So working only with the output from the model misses the general rule: the largest individual wave one can find will be a little less than twice the significant wave height. It does not mean that all waves encountered will be within the forecasted significant wave height; some will be less and some will be more because the measurement uses the Rayleigh statistical distribution model (García et al., 2009).

Consequently, the results produced by the SWAN model for the variables Hsig (significant wave height) and Hswell (significant swell height) will be used to calculate the seas variable; this variable is used to describe the combination of wave and swell heights when superimposed on one another, whose formula is:

$$seas = \sqrt{(Hsig^2 + Hswell^2)} \qquad (4)$$

Statistically, it is possible to generate a wave twice the size indicated by the Hsig every 8,000 seconds or 2.2 hours (Ainsworth, 2006); therefore we will use the seas result for the study.

To facilitate the results analysis, it was decided to use the lunar calendar as a basis due to its effects on the tide and on the earth's cycle of seasons. A fundamental part for the results validation will be the evidence in buoys and tide gauges; but it is the records on beaches and ports that stand out in importance, since there the wave height observed will give us a precise measure of what happened that can be contrasted with the simulations data. For the experiments that were carried out, the use of random numbers within the displacement formulas was not considered necessary because calculations of wave direction and height use them.

Development

The study area is located between (18.9º, 19.4º) north latitude and (-96.4º, -95.8º) west longitude, which includes the port and city of Veracruz, Boca del Rio and Antón Lizardo, among other sites of interest as indicated in Figure 2. The grid bathymetry has a 15 arc seconds resolution, or one point every 0.004º (GEBCO Compilation Group, 2021) which generates a mesh of 144 x 120 or 17,280 points that represent the study area and is showed in Figure 3; it should be noted that the bathymetry of the coastal zone (in blue) that suffers little alteration up to the land zone (in green). On the part of the unstructured mesh generated with Delaunay triangles, 1,715 vertices were obtained for the sea area with the generation conditions of internal angles of at least 30º and areas smaller than 100 m². 3,196 cells were generated, yielding 4,909 faces that were evaluated to obtain the height forecast. The simulation software is expected to provide data showing the variation in wave height near the beach, so it is necessary to confirm that the unstructured mesh has a higher density of triangles in coastal areas, as shown in Figure 4.

The next step was to obtain the 10 meters above sea level wind speed and speed direction as well as sea current speed and direction for the observed coordinates. The GEFS-Wave has both data, so the information extraction routines were programmed. For wind and tidal information, the data was entered for the point located at north latitude 19.15^o and west longitude -96.0^o; due to the area size and their availability because the GEFS-Wave outputs has 0.25^o resolution.

Each execution was carried out at 00, 03, 06, 09, 12, 15, 18 and 21 hours for each day, for a cycle of 3 months of temporary. The marine physics variables were considered with the default model values, as well as the GEN3 calculations offered by SWAN and the RIPPLES quotient was used for friction. For the tide calculations, the lunar calendars were used with the predicted height values for the different dates that were established for the experiment, those is published by Mexico's Secretary of Navy in the web page https://oceanografia.semar.gob.mx/mapa_estaciones.html.

Figure 2 Location study area. Secretary of Tourism, Veracruz, México
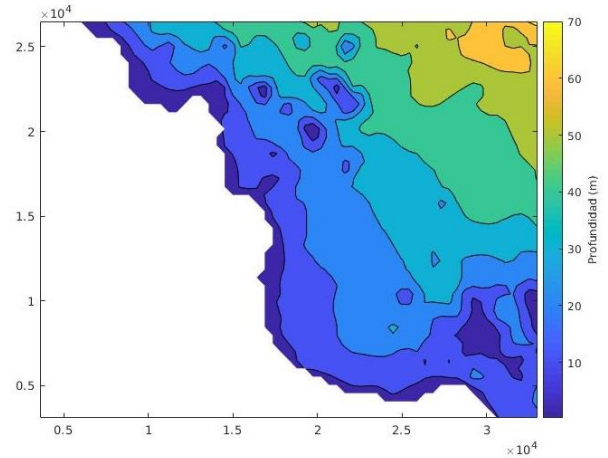
Figure 3 Area bathymetry, the land area is indicated in white and the ocean depth in blue to yellow scale
Source: Own elaboration
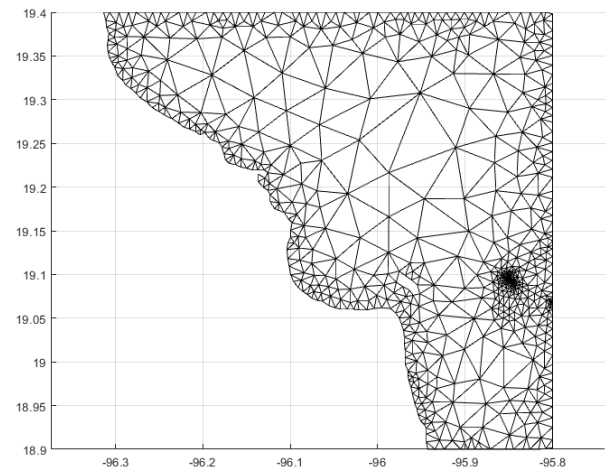
Figure 4 Study area map generated with Delaunay triangles
Source: Own elaboration

Once the input data (Delaunay diagram, bathymetry, waves and wind) had been obtained and the physics of the experiment had been configured, the next step was the recognition and validation of the information by the simulation software; the software output is shown in **Figure 5** and it was validated that they were consistent and it was possible to start the simulations cycle.

```
CGRID UNSTRUCTURED CIRCLE 36 0.0521 1.0 31
Resolution in sigma-space: df/f =  0.1000

READ UNSTRUCTURED TRIANGLE 'veracruz'

The unstructured grid contains solely triangles generated by Triangle

Number of vertices        =    1715

Number of cells           =    3196
    Number of internal cells =    2970
    Number of boundary cells =     226

Number of faces           =    4909
    Number of internal faces =    4679
    Number of boundary faces =     230

The minimum gridsize =      0.00001
The maximum gridsize =      0.06978


INPGRID BOTTOM -96.40 18.9 0 143 119 0.004166 0.004166

$>INPGRID BOTTOM UNSTRUCTURED

READINP BOTTOM -1 'veracruz.bot' 2 6
** Heading lines file veracruz.bot **
-> ncols        144
-> nrows        120
-> xllcorner    -96.400000000000
-> yllcorner    18.900000000000
-> cellsize     0.004166666667
-> NODATA_value -32767
```

Figure 5 Information from the SWAN software indicating the recognition of the input data to perform the simulation
Source: Own elaboration

To establish a reference, the data recorded by the buoys and the tide gauges placed in the port of Veracruz were taken. The variable that was compared was the height of the wave, since with it the possibility of the sea exceeding the height of the natural or artificial barriers and invading the land was determined. In this project it was determined not to use the variable of wind direction or construction plans and it is assumed that the bordering areas of the beach area are considered in the altimetry, due to the lack of reports of constructions or artificial barriers that stop the straight ahead of the waves. The experiments to adjust the physics parameters of the model were applied for the year 2021. The most observed variables were those related to the friction and density of the water (because it is a deep-water port with oil contamination). As shown in Table 1 for a control point located at north latitude 19.21° west longitude -96.12° which is the closest point to the Ver2 buoy. The data shown is illustrative and indicates how the data from the different runs was compared against the buoy reading.

Table: control01, SWAN version:41.31				
Friction/date	**Xp (deg)**	**Yp (deg)**	**Hsig (m)**	**Tm01 (s)**
(03/31)				
JONSWAP	-96.12	19.21	1.473	12.018
RIPPLES	-96.12	19.21	1.588	13.155
BUOY	Ver2		1.541	12.868
(06/30)				
JONSWAP	-96.12	19.21	1.488	12.787
RIPPLES	-96.12	19.21	1.396	12.644
BUOY	Ver2		1.432	11.873
(09/30)				
JONSWAP	-96.12	19.21	2.837	14.982
RIPPLES	-96.12	19.21	3.573	13.872
BUOY	Ver2		3.143	12.832
(12/31)				
JONSWAP	-96.12	19.21	0.929	11.193
RIPPLES	-96.12	19.21	1.388	11.627
BUOY	Ver2		1.113	11.521

Table 1 Result comparison of the SWAN software executions against the records in buoys
Source: Own elaboration

Due to the differences, it was found that the RIPPLES friction was the closest for the wave height measurements under the conditions that were established.
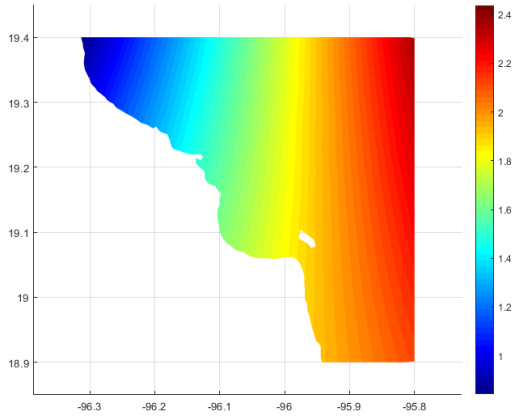
Some of the problems reported were the interpretation of the data produced by the SWAN simulator as well as the way in which it needs the input data to make the calculations on the wave's height considering the tide and the wind waves. One of the errors that appeared in the diagrams was the effect of wave tidal continuity. This is due to the fact that the data entered as a start has greater relevance in the final results than the calculations per se; so it was necessary to consider the results of the first execution as start results prepared for the rest of the executions. Figure 6 and 7 shows some errors clearly.

Once the outputs of the simulations were accepted, the value of H was replaced in equations 2 and 3 by the results obtained for seas to perform the calculation for the particles movement.
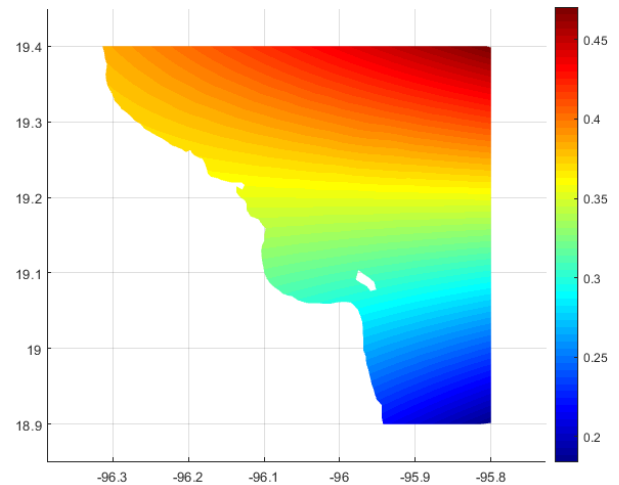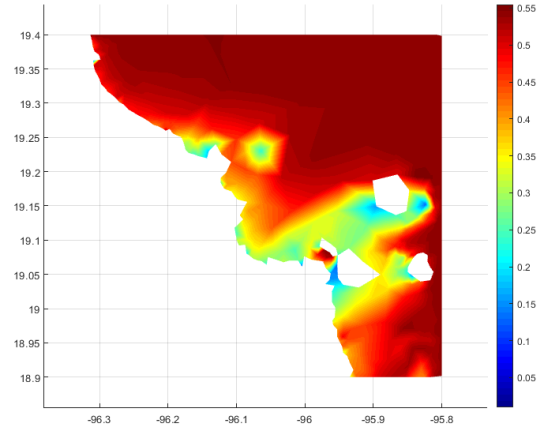

Figure 6 Tidal wave high diagram generated considering a uniform value for the area. The label bar has the same colour scheme as the map
Source: Own elaboration

AGUILERA-MENDEZ, José María, JUAREZ-TOLEDO, Carlos, MARTINEZ-CARRILLO, Irma and VERA-POPOCA, Roberto Ismael. Use of unstructured meshes for wave height and particles horizontal displacement analysis in central zone Veracruz, Mexico. ECORFAN Journal-Taiwan. 2022

Figure 7 Tidal wave high diagram generated using a non-constant swell input values with different grid scales
Source: Own elaboration

Results

With the results obtained for Hsig and Hswel variables at the time of adjusting the simulation physics and data grid input and was validated against equation 1, it only remained to apply the formula for obtaining seas variable value, equation 4, for the different control points. The Ver2 buoy checkpoint results are shown below in Table 2:

Table: Results01, SWAN version:41.31AB				
Date	Hsig	Hswel	seas	buoy
01/10	1.5893	0.1976	1.6015	2.089
01/11	1.9837	0.2467	1.9989	2.108
01/12	1.6832	0.2093	1.6961	1.967
01/13	2.1233	0.2640	2.1396	2.472
01/14	2.4428	0.3038	2.4616	2.278
02/20	0.73153	0.09126	0.7372	0.8367
02/21	0.32296	0.04014	0.3254	0.4921
02/22	0.66603	0.07802	0.6705	0.6252
02/23	0.13386	0.01923	0.1352	0.1593

Table 2 The data obtained for wave height and seas variable calculation are shown. The buoy height presented is the maximum height reached in the same observation period that was from 12:00 to 14:59 (12Z). Data in meters (m)
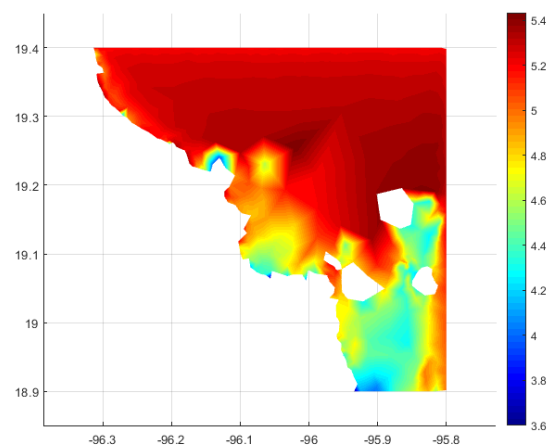*Source: Own elaboration*
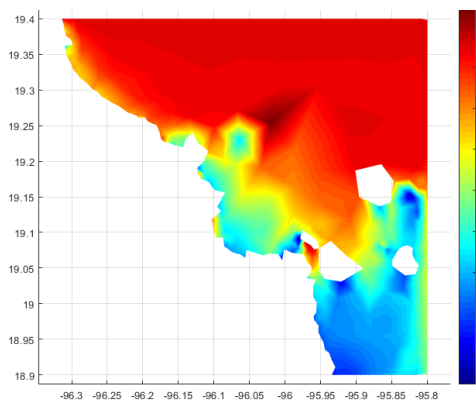
Figure 8 The seas variable behavior is shown as the probable maximum wave height with north originated winds
Source: Own elaboration

Figure 9 The seas variable behavior is shown as the probable maximum wave height with west originated winds
Source: Own elaboration

With the data obtained for wave height, proceeded to verify, in the same tabulated way, the information on the wave frequency showed in **Table 3**.

| Table: Results02, SWAN version:41.31AB		
Date	Tm01 (s)	Buoy (s)
01/10	8.45	8.56
01/11	7.98	8.23
01/12	8.24	7.64
01/13	8.42	7.32
01/14	7.78	7.84
02/20	6.25	6.03
02/21	5.99	6.21
02/22	6.14	5.93
02/23	5.20	5.31

Table 3 Wave frequency as result of the simulation against the data buoy recorded
Source: Own elaboration

With which it was possible to generate the wave frequency maps as Figure 10

Figure 10 Wave period
Source: Own elaboration

Once the data were obtained, it was possible to substitute the values in the horizontal particle displacement equation and perform the analysis on free-floating bodies, such as some types of algae, as well as floating debris (garbage). The accumulated data allowed us to construct spaghetti-type diagrams that allow us to make an approximate calculation of the movement of objects on the ocean surface. An accumulation of data is mentioned since a spaghetti diagram reflects the possible change in the path of a body, and this change cannot be reflected only in time t; a sequence of t, t+1, t+2… t+n is required to indicate the expected change.
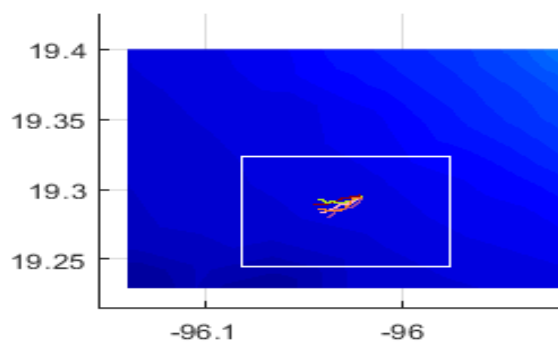
Figure 11 Spaghetti diagram showing possible particle displacements for a specific point for times t, t+1, t+2...t+24
Source: Own elaboration

Conclusions

The results showed a high percentage of acceptance with respect to the values recorded by the tide gauges and buoys, showing a variation within 20%. As also explained, in some cases the size of the wave doubled the predicted size; but for the data that was available, it was only possible on occasions where the presence of hurricanes or tropical storms drastically affected the results.

The particles horizontal displacement showed great consistency with the movement of floating objects that were in the area, but it was not possible to validate them mainly due to the lack of information from the authorities; although laboratory results with satellite images indicated a good correlation.

Just as the software considers variables for the experiment physics, it would also be advisable to have several data sources that could be introduced into the experiment, thus not only having data from SEMAR and NOAA.

Likewise, for further research, the use of non-hydrostatic, free-surface, rotational flow and transport phenomena in coastal waters models is suggested; such as SWASH, XB and ADCIR, among others.

The experiment showed consistency with the available data and scales; It would be advisable to have more sensitive bathymetry data and a smaller area (less than 100 km^2) if the objective was to analyze the waves height and their approach or invasion of beach or inland areas. It is recommended to use Artificial Intelligence tools like Artificial Neural Network that allow the learning of images (Aguilera-Méndez, Juárez-Toledo, Martínez-Carrillo, & Flores-Vázquez, 2021) to be used in research or civil protection areas in the event of rising waves in beach areas.

References

Aguilera-Méndez, J. M., Juárez-Toledo, C., Martínez-Carrillo, I., & Flores-Vázquez, A. L. (2021). Meteorological patterns recognition using Artificial Neural Networks programmed with the Swish activation function. *Revista de Tecnologías Computacionales*, *5*(15), 21–28. https://doi.org/10.35429/JOCT.2021.15.5.21.28

Aguilera-Méndez, J. M., Juárez-Toledo, C., Martínez-Carrillo, I., & Vera-Popoca, R. I. (2021). Generation of unstructured meshes using Delaunay triangles for tidal analysis of the port of Acapulco, Mexico. *Revista de Simulación y Laboratorio*, *8*(24), 20–27. https://doi.org/10.35429/JSL.2021.24.8.20.27

Ainsworth, T. (2006). When Do Ocean Waves Become "Significant"? A Closer Look at Wave Forecasts. *Mariners Weather Log*. https://www.vos.noaa.gov/MWL/apr_06/waves.shtml

Friedman, J., & Tillich, J.-P. (2004). Wave equations for graphs and the edge-based Laplacian. *Pacific Journal of Mathematics*, *216*(2), 229–266. https://doi.org/10.2140/pjm.2004.216.229

García, F., Palacio, C., & Garcia, U. (2009). Unestructured Mesh Generation for Numeric Models Implementation. *Dyna*, *76*(157), 17–25.

GEBCO Compilation Group. (2021). *GEBCO*. https://doi.org/10.5285/c6612cbe-50b3-0cff-e053-6c86abc09f8f

Johns, E. M., Lumpkin, R., Putman, N. F., Smith, R. H., Muller-Karger, F. E., T. Rueda-Roa, D., Hu, C., Wang, M., Brooks, M. T., Gramer, L. J., & Werner, F. E. (2020). The establishment of a pelagic Sargassum population in the tropical Atlantic: Biological consequences of a basin-scale long distance dispersal event. *Progress in Oceanography*, *182*(September 2019), 102269. https://doi.org/10.1016/j.pocean.2020.102269

Musinguzi, A., Akbar, M. K., Fleming, J. G., & Hargrove, S. K. (2019). Understanding Hurricane Storm Surge Generation and Propagation Using a Forecasting Model, Forecast Advisories and Best Track in a Wind Model, and Observed Data—Case Study Hurricane Rita. *Journal of Marine Science and Engineering*, *7*(3), 77. https://doi.org/10.3390/jmse7030077

Pecher, A., & Kofoed, J. P. (Eds.). (2017). *Handbook of Ocean Wave Energy* (Vol. 7). Springer International Publishing. https://doi.org/10.1007/978-3-319-39889-1

Ringler, T., Petersen, M., Higdon, R. L., Jacobsen, D., Jones, P. W., & Maltrud, M. (2013). A multi-resolution approach to global ocean modeling. *Ocean Modelling*, *69*, 211–232. https://doi.org/10.1016/j.ocemod.2013.04.010

Toth, Z., & Kalnay, E. (1997). Ensemble Forecasting at NCEP and the Breeding Method. *Monthly Weather Review*, *125*(12), 3297–3319. https://doi.org/10.1175/1520-0493(1997)125<3297:EFANAT>2.0.CO;2

Weatherill, N. P. (1992). Delaunay triangulation in computational fluid dynamics. *Computers & Mathematics with Applications*, *24*(5–6), 129–150. https://doi.org/10.1016/0898-1221(92)90045-J

BFO films obtained by Spray Pyrolysis optical and structural analysis

Análisis óptico y estructural de películas de BFO obtenidas por Spray Pirólisis

HERNÁNDEZ-SIMÓN, Zaira Jocelyn†, LUNA-LÓPEZ, José Alberto*, HERNÁNDEZ-DE LA LUZ, Álvaro David and MENDOZA-CONDE, Gabriel Omar

Centro de Investigaciones en Dispositivos Semiconductores (CIDS-ICUAP), Benemérita Universidad Autónoma de Puebla (BUAP), Col. San Manuel, Cd. Universitaria, Av. San Claudio y 14 Sur, Edificios IC5 y IC6, Puebla, Pue., 72570, México.

ID 1st Author: *Zaira Jocelyn, Hernández-Simón* / **ORC ID:** 0000-0003-4185-4101, **CVU CONACYT ID:** 774431

ID 1st Co-author: *José Alberto, Luna-López* / **ORC ID:** 0000-0002-7647-3184, **CVU CONACYT ID:** 200808

ID 2nd Co-author: *José Álvaro David, Hernández-de la Luz* / **ORC ID:** 0000-0002-7913-0240, **CVU CONACYT ID:** 240901

ID 3rd Co-author: *Gabriel Omar, Mendoza-Conde* / **ORC ID:** 0000-0001-5451-9770, **CVU CONACYT ID:** 774931

Abstract

In the present research work, the obtaining of $BiFeO_3$ films using the ultrasonic Spray Pyrolysis technique is reported. The deposited films were characterized optically and structurally, showing interesting results, such as the formation of column-type microstructured arrangements with an average height of 805 nm, as well as the presence of 2 predominant phases in the material, the combination of rhombohedral $BiFeO_3$ with tetragonal Bi_2O_3, in addition to the tetragonal $Bi_{36}Fe_2O_{57}$ phase. From the diffraction patterns, the lattice parameters were also obtained, with which the crystalline structure of each phase was graphically represented, the average crystallite size was calculated using the Scherrer formula with an average size of 13 nm, which could benefit the Magnetic properties of $BiFeO_3$. The film also shows a band gap shift at lower energies, which is an improvement for future applications in the field of photovoltaics, furthermore these films were obtained with a simple and economical technique using a deposition temperature of only 100°C.

Resumen

En el presente trabajo de investigación se reporta la obtención de películas de $BiFeO_3$ utilizando la técnica de Spray Pyrolysis ultrasónico, las películas depositadas fueron caracterizadas óptica y estructuralmente mostrando resultados interesantes, como la formación de arreglos microestructurados de tipo columna con una altura promedio de 805 nm, así como la presencia de 2 fases predominantes en el material, la combinación de $BiFeO_3$ romboédrico con Bi_2O_3 tetragonal, además de la fase $Bi_{36}Fe_2O_{57}$ tetragonal. De los patrones de difracción también fueron obtenidos los parámetros de red, con lo cual se representó gráficamente la estructura cristalina de cada fase, los tamaños de cristalito promedio fueron calculados utilizando la fórmula de Scherrer con tamaños promedio de 13 nm, lo cual podría beneficiar las propiedades magnéticas del $BiFeO_3$. La película, además, muestra un corrimiento del band gap a menores energías, lo cual es beneficioso para futuras aplicaciones en el campo de la fotovoltaica, además estas películas fueron obtenidas con una técnica sencilla y económica usando una temperatura de depósito de sólo 100°C.

BiFeO₃, Structural characterization, Spray pyrolysis

BiFeO₃, Caracterización structural, Spray Pirolisis

* Correspondence to Author (E-mail: jose.luna@correo.buap.mx)
† Researcher contributing as first author.

Introduction

As well known, multiferroics are interesting materials which exhibits at least two of the ferroic properties in the same phase and exhibit a coupling effect between the ferroic properties [1].

Among many ferroelectric materials, $BiFeO_3$ (BFO) is one of the key research materials due to its large remanent polarization ($\sim$100 $\mu C/cm^2$), high Curie temperature ($\sim$810 °C) and narrow direct band gap ($\sim$2.7 eV) [2], whereby it has significant absorption of visible light, which is beneficial for the development of solar energy devices [3]. Nevertheless, the major challenge on $BiFeO_3$ based photovoltaic devices is low photovoltaic output, which is affected by their intrinsic ferroelectric photovoltaic mechanism [4].

Besides to photovoltaic applications, the BFO has also applications in the field of spintronics, sensors and new data storage devices. [5].

Many physical and chemical methods have been used to obtain BFO films, including radio-frequency sputtering, molecular beam epitaxy, pulsed laser deposition, chemical (sol–gel) solution deposition, and hydrothermal synthesis, have been employed for the deposition of BFO thin films. Notwithstanding, these deposition techniques are highly expensive, and it is required long time for deposition process. On the other hand, spray pyrolysis is a very simple and inexpensive deposition technique for thin films fabrication, and it has potential for large scale preparation. Additionally, precise control of composition and better chemical homogeneity are possible in this deposition technique [6].

The growing condition which allows a pure and stoichiometric BFO phase to be obtained is always very narrow, so that very small changes in the deposition parameters can lead to either major changes in the film's properties or to the nucleation of spurious phases. The BFO films have been reported to present a magnetic moment arising from parasitic phases formed mainly by iron oxides [7].

In the case of impurity phases that present an excess of bismuth, such as $Bi_{25}FeO_{39}$ or the combination of BFO with B_2O_3, a great interest has recently arisen in their formation, due to investigations that report the superior photocatalytic action that they exhibit [8] along with good photoelectric response.

Description of the method

The BFO films were deposited using the Spray Pyrolysis technique, the deposit temperature used was 100°C and for preparing the precursor solution a molarity of 0.6 M was used, it was required as a first step to use a reaction for which the following reagents were used; Iron nitrate nonahydrate 98% and Bismuth Nitrate pentahydrate

Causing the following reaction:

$Fe(NO_3)_3 * 9 H_2O + Bi (NO_3)_3 * 5 H_2O \longrightarrow BiFeO_3 + 6 (HNO_3) + 11 H_2O$
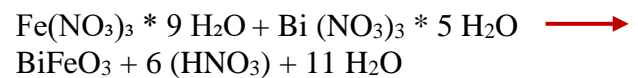
The deposition time used was 10 minutes and the deposition were carried out on an n-type silicon substrate with a resistivity of 1-10 Ω, orientation (1 0 0), the deposit distance between the hot wall and the substrate was 4 cm.

After the deposit, a thermal annealing of 500°C was carried out in accordance with what was reported by [9], in that investigation annealing at higher temperatures was carried out, resulting in the emergence of phases $Bi_2Fe_4O_9$ and $Bi_{25}FeO_{39}$ at 700°C temperature and at temperatures higher than 800°C there is a decrease in the phase $Bi_{25}FeO_{39}$ and the phase $Bi_2Fe_4O_9$ becomes dominant.

To structurally characterize the obtained film, profilometry measurements were made in a Dektak 150 profilometer with a vertical tracking resolution of 1 Å, SEM measurements were also made with a JEOL JSM-5300 equipment applying 20kV. Finally, grazing incidence X-ray diffraction measurements, with an angle θ-2θ of 1° using a Bruker D8 Venture equipment was carried out.

To obtain the optical properties of the material, diffuse reflectance and absorbance measurements were made using a Varian Cary 5000 UV-Vis-NIR spectrophotometer. Finally, the obtained structures were modeled using the Diamond 4 Cristal and molecular structure visualization software.

HERNÁNDEZ-SIMÓN, Zaira Jocelyn, LUNA-LÓPEZ, José Alberto, HERNÁNDEZ-DE LA LUZ, Álvaro David and MENDOZA-CONDE, Gabriel Omar. BFO films obtained by Spray Pyrolysis optical and structural analysis. ECORFAN Journal-Taiwan. 2022

Results

In Figure 1, a photograph of the appearance of the film obtained without close-ups is presented in the upper left part, while in the lower part a photograph of the film taken with microscope magnification is shown with the presence of small clusters within the film.
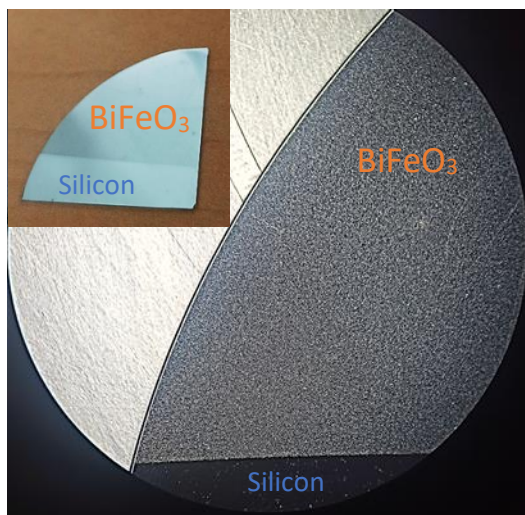

Figure 1 Image of the film obtained using the spray pyrolysis technique

In order to properly analyze the thickness and morphology of the film, Graphic 1 shows the thickness profile obtained by profilometry, where column-type microstructured arrangements with an average height of 805 nm can be observed, the separation among these growths has micron variations where the growth of a thin film of BFO with a thickness of approximately 150 nm is also observed.
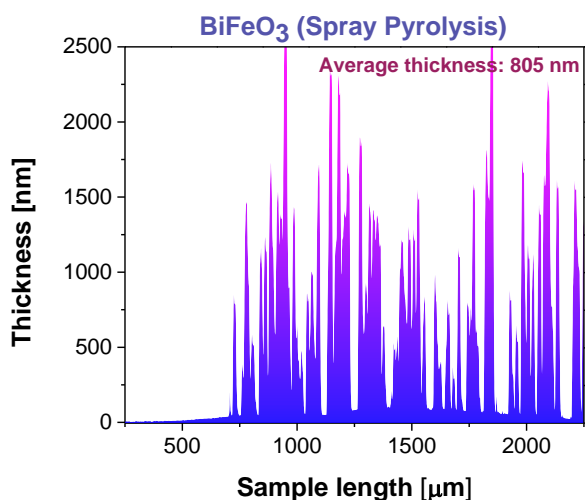
Graphic 1 Thickness profile and average thickness for the BFO film deposited by Spray Pyrolysis
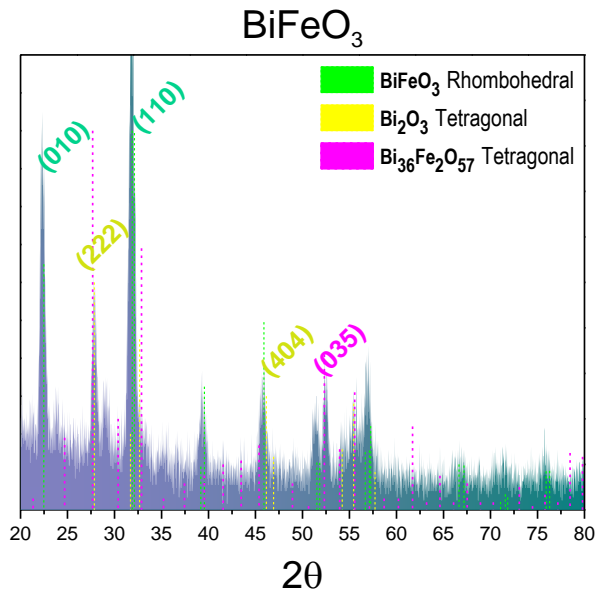
Figure 2 present the SEM micrographs obtained from the film, where subsection a) shows the presence of the columns observed by profilometry and their distribution fully coincides with the profile obtained from the sample, also in part b) it is shown a magnification x2000 where these columns have a circular shape with a variable diameter, but with an average of 5 μm.
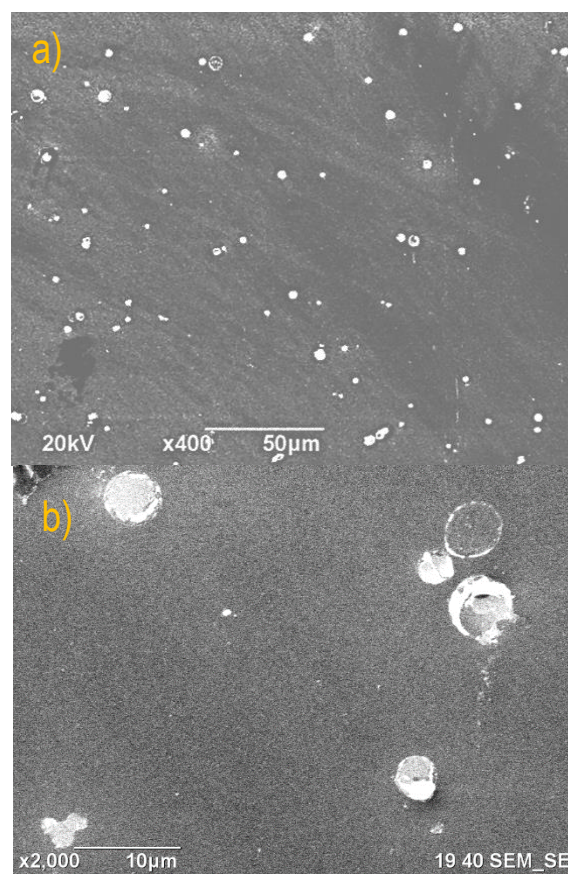
Figure 2 Micrographs of the BFO film obtained by SEM with different magnifications.

Graphic 2 shows the diffraction pattern, where we present the rhombohedral phase of $BiFeO_3$ with a preferential orientation in the (110) plane, it is also observed that there is a mixture with the tetragonal phase of Bi_2O_3 which presents a preferential orientation in the plane (222).

Both phases present in the film correspond to the structure at room temperature for each case. Finally, the presence of the tetragonal phase of $Bi_{36}Fe_2O_{57}$ with a preferential orientation in the (035) plane is also observed to a lesser extent.

HERNÁNDEZ-SIMÓN, Zaira Jocelyn, LUNA-LÓPEZ, José Alberto, HERNÁNDEZ-DE LA LUZ, Álvaro David and MENDOZA-CONDE, Gabriel Omar. BFO films obtained by Spray Pyrolysis optical and structural analysis. ECORFAN Journal-Taiwan. 2022

Graphic 2 Diffractogram of BFO deposited by Spray Pyrolysis and diffraction patterns of rhombohedral $BiFeO_3$, tetragonal Bi_2O_3 and tetragonal $Bi_{36}Fe_2O_{57}$

Figure 3 shows a structural representation of the phases and materials obtained using the lattice parameters found in the diffraction pattern of the film obtained by spray pyrolysis.

The lattice parameters are as follows:

$BiFeO_3$ a= 3.952 Å, b= 3.952 Å, c= 3.952 Å y $\alpha=\beta=\gamma= 89.6°$.

B_2O_3 a= 7.7299 Å, b= 7.7299 Å, c= 5.6587 Å y $\alpha=\beta=\gamma= 90°$.

$Bi_{36}Fe_2O_{57}$ a= 10.184 Å, b= 10.184 Å, c= 10.184 Å y $\alpha=\beta=\gamma= 90°$.

From the diffraction pattern, mean crystallite sizes are calculated using the Scherrer's formula from the broadening of the peaks.

Scherrer's formula is:

$$t = \frac{K\lambda}{\beta\cos\theta} \qquad (1)$$

Where t is the crystallite size, K is Scherrer's constant (0.94), λ is the wavelength of the radiation source (1.59 Å), β is the full width at half maximum, and θ is the angle of Bragg [10].
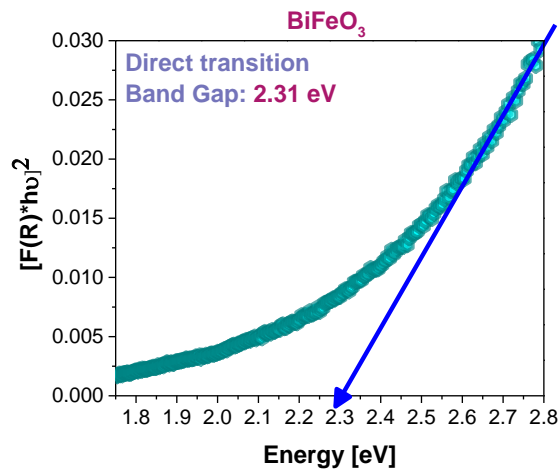
The results obtained show an average crystallite diameter of approximately 13 nm for BFO, as well as for Bi_2O_3.
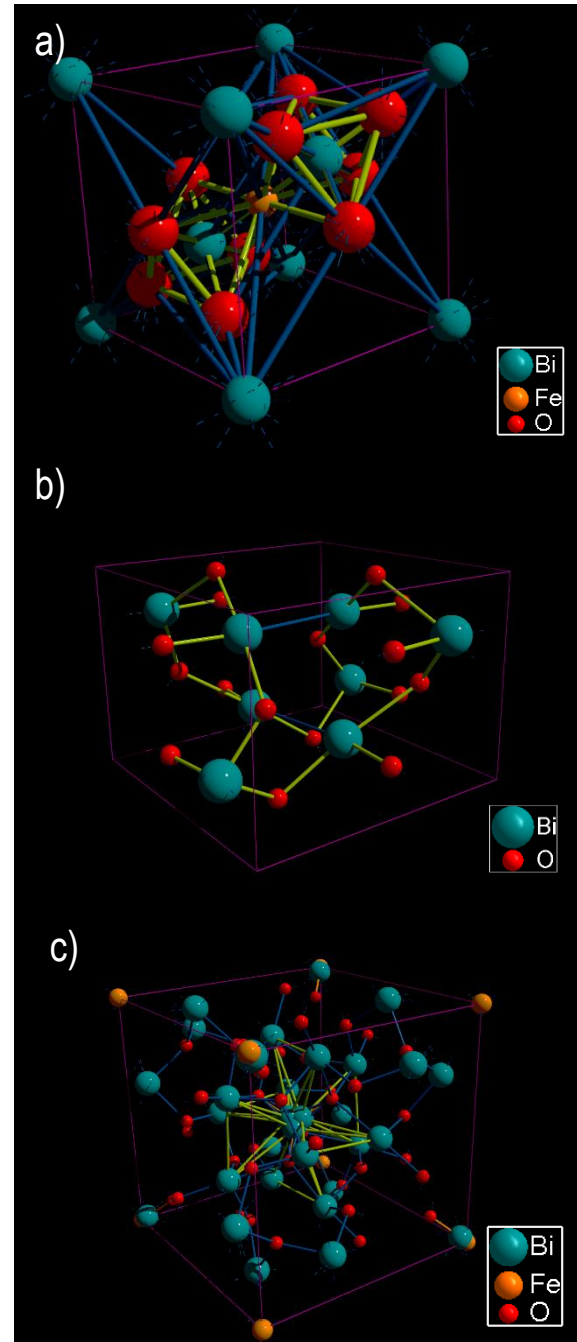
Figure 3 Representation of the different phases present in the obtained film a) $BiFeO_3$ rhombohedral, b) Bi_2O_3 tetragonal, c) $Bi_{36}Fe_2O_{57}$ tetragonal

Regarding to the optical properties of the material, Graphic 3 shows the band gap calculated by means of diffuse reflectance measurements and the use of the Kubelka-Munk function [11] where a direct type transition was used in accordance with what was reported for the BFO [12].

The band gap obtained corresponds to 2.31 eV, so there is a shift in the band gap of the material towards lower energies.

HERNÁNDEZ-SIMÓN, Zaira Jocelyn, LUNA-LÓPEZ, José Alberto, HERNÁNDEZ-DE LA LUZ, Álvaro David and MENDOZA-CONDE, Gabriel Omar. BFO films obtained by Spray Pyrolysis optical and structural analysis. ECORFAN Journal-Taiwan. 2022

Graphic 3 Band gap of the BFO film calculated by the Kubelka-Munk function using a direct transition

Analysis

From the X-ray diffractograms it is observed as mentioned above, that in the film deposit we obtain the rhombohedral phase of $BiFeO_3$ in combination with the tetragonal phase of Bi_2O_3 and to a lesser extent the $Bi_{36}Fe_2O_{57}$ in tetragonal phase. Spectra such as the ones obtained have been reported in investigations where the union of $BiFeO_3$-Bi_2O_3 films is analyzed [13], as well as the heterojunction of nanofibers and other composites of these 2 materials [14]. These results, together with those obtained by SEM, could indicate that a $BiFeO_3$ film is actually being obtained, so $BiFeO_3$ is embedded with Bi_2O_3 (clusters or columns observed in figure 2), although according to the size of the crystallites, this mixture of phases could be considered to be at the nanometric level with nanocrystalline embedding. This result is very interesting from the magnetic point of view since it has been reported [12] that the magnetic properties in BFO increase as the crystallite size decreases.

Regarding the $Bi_{36}Fe_2O_{57}$ phase, it is reported that small amounts of bismuth-rich secondary phases such as $Bi_{40}Fe_2O_{63}$ and $Bi_{36}Fe_2O_{57}$ are commonly found in polycrystalline samples of $BiFeO_3$ and the segregation of these secondary phases at the grain boundaries could play a role in reducing the resistivity of the material. The low resistivity, and resulting low bias inhibit the ferroelectric hysteresis loop [15].

The $Bi_{36}Fe_2O_{57}$ phase, as well as the Bi_2O_3 phase, indicate an excess of bismuth in our film, which could be explained in terms of the low deposition temperature of 100°C used and the heat annealing carried out at 500°C.

The Bi_2O_3 is a p-type bismuth-based semiconductor with unique physical and chemical characteristics which make it promising in photoelectric applications, it has a band gap of 2.2 to 2.8 eV and shows good absorption in the visible region of the light [14]. According to the results published by [16], $BiFeO_3$ is a typical n-type semiconductor, so the heterojunction of Bi_2O_3/$BiFeO_3$ forms a p-n junction type compound, thus the photogenerated charges are effectively separated and transferred at the interface of Bi_2O_3 and $BiFeO_3$ [14].

Furthermore, a high photovoltaic performance in $BiFeO_3$ films by manipulating the concentration of their oxygen vacancies through the alteration of the Bi content has been reported, the results of this research show that the highest photovoltaic production was achieved in $Bi_{1.05}FeO_3$ films, whose response is 1000 times better than that of $Bi_{0.95}FeO_3$ films, as a charge balance requirement in BFO, Bi vacancies lead to an increase in the oxygen vacancy concentration, while an excess of Bi is linked to a decrease in the oxygen vacancy concentration [17].

Analyzing the shift of the band gap obtained towards lower energies, this can be attributed to the mixture of phases with the insertion of Bi_2O_3 in the BFO molecular structure present in the film, which again corroborates what is observed from the diffractogram of Graph 2, this shift is also beneficial for light absorption according to what was reported in [13] where the decrease in the band gap is obtained by doping the BFO, so in our case the presence of important quantities of Bi_2O_3 molecules causes the reduction of the bandgap energy of the film.

In this context, it is easy to discern that obtaining the reported $BiFeO_3$-Bi_2O_3 film represents an enormous advantage in terms of materials that are to be applied in the field of photovoltaics (both in solar cells and photocatalytic applications), since it is a film with both phases well defined, besides to the fact that the deposit technique is simple and economical when using the pyrolysis spray system.

HERNÁNDEZ-SIMÓN, Zaira Jocelyn, LUNA-LÓPEZ, José Alberto, HERNÁNDEZ-DE LA LUZ, Álvaro David and MENDOZA-CONDE, Gabriel Omar. BFO films obtained by Spray Pyrolysis optical and structural analysis. ECORFAN Journal-Taiwan. 2022

Conclusions

In the present research, the obtaining of $BiFeO_3$-Bi_2O_3 films by means of the ultrasonic Spray Pyrolysis technique is reported, with the formation of 2 phases in the material, namely, $BiFeO_3$ with a rhombohedral structure and Bi_2O_3 with a tetragonal phase, additionally to the presence of the tetragonal $Bi_{36}Fe_2O_{57}$ phase, this is indicative of an excess bismuth in the material possibly attributed to the low deposition temperature. Obtaining this type of structures by the ultrasonic Spray Pyrolysis technique is so important for future photoelectric applications due to the various investigations are focused on obtaining this type of arrangement by sophisticated techniques. The reported structures possess an excellent response to light, such fact makes them good candidates to improving photovoltaic cells based on multiferroic materials.

Funding

References

[1] Wang, F., Lv, S., Fu, C., & Zhang, C. (2017). The first-principles calculations on trigonal and hexagonal structures of BiFeO3. Ferroelectrics, 520(1), 177-18. https://doi.org/10.1080/00150193.2017.1388763

[2] Chen, G., Chen, J., Pei, W., Lu, Y., Zhang, Q., Zhang, Q., & He, Y. (2019). Bismuth ferrite materials for solar cells: current status and prospects. Materials Research Bulletin, 110, 39-49. https://doi.org/10.1016/j.materresbull.2018.10.011

[3] Heo, Y., & Alexe, M. (2022). Boosting Piezoelectricity under Illumination via the Bulk Photovoltaic Effect and the Schottky Barrier Effect in BiFeO3. Advanced Materials, 34(5), 2105845. https://doi.org/10.1002/adma.202105845

[4] Yang, T., Wei, J., Sun, Z., Li, Y., Liu, Z., Xu, Y., ... & Cheng, Z. (2022). Design of oxygen vacancy in BiFeO3-based films for higher photovoltaic performance. Applied Surface Science, 575, 151713. https://doi.org/10.1016/j.apsusc.2021.151713

[5] Wu, J., Fan, Z., Xiao, D., Zhu, J., & Wang, J. (2016). Multiferroic bismuth ferrite-based materials for multifunctional applications: ceramic bulks, thin films and nanostructures. Progress in Materials Science, 84, 335-402. https://doi.org/10.1016/j.pmatsci.2016.09.001

[6] Razad, P. M., Saravanakumar, K., Ganesan, V., Choudhary, R. J., Moses Ezhil Raj, A., Devaraj, R., ... & Sanjeeviraja, C. (2017). Novel report on single phase BiFeO3 nanorod layer synthesised rapidly by novel hot-wall spray pyrolysis system: evidence of high magnetization due to surface spins. Journal of Materials Science: Materials in Electronics, 28(4), 3217-3225. https://doi.org/10.1007/s10854-016-5911-5

[7] Mori, T. J., Mouls, C. L., Morgado, F. F., Schio, P., & Cezar, J. C. (2017). Parasitic phases at the origin of magnetic moment in BiFeO3 thin films grown by low deposition rate RF sputtering. Journal of Applied Physics, 122(12), 124102. https://doi.org/10.1063/1.5003764

[8] Margha, F. H., Radwan, E. K., Badawy, M. I., & Gad-Allah, T. A. (2020). Bi2O3–BiFeO3 glass-ceramic: controllable β-/γ-Bi2O3 transformation and application as magnetic solar-driven photocatalyst for water decontamination. ACS omega, 5(24), 14625-14634. https://doi.org/10.1021/acsomega.0c01307

[9] Ryu, J., Baek, C. W., Park, D. S., & Jeong, D. Y. (2010). Multiferroic BiFeO3 thick film fabrication by aerosol deposition. Metals and Materials International, 16(4), 639-642. https://doi.org/10.1007/s12540-010-0818-9

[10] Afzal, A. M., Umair, M., Dastgeer, G., Rizwan, M., Yaqoob, M. Z., Rashid, R., & Munir, H. S. (2016). Effect of O-vacancies on magnetic properties of bismuth ferrite nanoparticles by solution evaporation method. *Journal of Magnetism and Magnetic Materials*, *399*, 77-80. https://doi.org/10.1016/j.jmmm.2015.09.06 2

[11] Jamil, H., Dildar, I. M., Ilyas, U., Hashmi, J. Z., Shaukat, S., Sarwar, M. N., & Khaleeq-ur-Rahman, M. (2021). Microstructural and Optical study of polycrystalline manganese oxide films using Kubelka-Munk function. *Thin Solid Films*, *732*, 138796. https://doi.org/10.1016/j.tsf.2021.138796

[12] Liang, K. Y., Wang, Y. F., Yang, Z., Zhang, S. P., Jia, S. Y., & Zeng, J. H. (2021). Above-Band-Gap Voltage from Oriented Bismuth Ferrite Ceramic Photovoltaic Cells. ACS Applied Energy Materials, 4(11), 12703-12708. https://doi.org/10.1021/acsaem.1c02395

[13] Yan, X., Pu, R., Xie, R., Zhang, B., Shi, Y., Liu, W., ... & Yang, N. (2021). Design and fabrication of Bi2O3/BiFeO3 heterojunction film with improved photoelectrochemical performance. Applied Surface Science, 552, 149442. https://doi.org/10.1016/j.apsusc.2021.1494 42

[14] Duan, F., Ma, Y., Lv, P., Sheng, J., Lu, S., Zhu, H., ... & Chen, M. (2021). Oxygen vacancy-enriched Bi2O3/BiFeO3 pn heterojunction nanofibers with highly efficient photocatalytic activity under visible light irradiation. Applied Surface Science, 562, 150171. https://doi.org/10.1016/j.apsusc.2021.1501 71

[15] Nikumaa, M. (2011). Solid solution in the systems BiMO3-ATiO3 (M= Fe, Cr; A= Ba, Sr) synthesis, structure and magnetic properties (Master's thesis). https://hdl.handle.net/20.500.12380/146774

[16] Ma, Y., Lv, P., Duan, F., Sheng, J., Lu, S., Zhu, H., ... & Chen, M. (2020). Direct Z-scheme Bi2S3/BiFeO3 heterojunction nanofibers with enhanced photocatalytic activity. Journal of Alloys and Compounds, 834, 155158. https://doi.org/10.1016/j.jallcom.2020.1551 58

[17] Yang, T., Wei, J., Guo, Y., Lv, Z., Xu, Z., & Cheng, Z. (2019). Manipulation of oxygen vacancy for high photovoltaic output in bismuth ferrite films. ACS applied materials & interfaces, 11(26), 23372-23381. https://doi.org/10.1021/acsami.9b06704

[Title in Times New Roman and Bold No. 14 in English and Spanish]

Surname (IN UPPERCASE), Name 1st Author†*, Surname (IN UPPERCASE), Name 1st Co-author, Surname (IN UPPERCASE), Name 2nd Co-author and Surname (IN UPPERCASE), Name 3rd Co-author

Institutional Affiliation of Author including Dependency (No.10 Times New Roman and Italic)

International Identification of Science - Technology and Innovation

ID 1st Author: (ORC ID - Researcher ID Thomson, arXiv Author ID - PubMed Author ID - Open ID) and CVU 1st author: (Scholar-PNPC or SNI-CONACYT) (No.10 Times New Roman)

ID 1st Co-author: (ORC ID - Researcher ID Thomson, arXiv Author ID - PubMed Author ID - Open ID) and CVU 1st co-author: (Scholar or SNI) (No.10 Times New Roman)

ID 2nd Co-author: (ORC ID - Researcher ID Thomson, arXiv Author ID - PubMed Author ID - Open ID) and CVU 2nd co-author: (Scholar or SNI) (No.10 Times New Roman)

ID 3rd Co-author: (ORC ID - Researcher ID Thomson, arXiv Author ID - PubMed Author ID - Open ID) and CVU 3rd co-author: (Scholar or SNI) (No.10 Times New Roman)

Abstract (In English, 150-200 words)

Objectives
Methodology
Contribution

Keywords (In English)

Indicate 3 keywords in Times New Roman and Bold No. 10

Abstract (In Spanish, 150-200 words)

Objectives
Methodology
Contribution

Keywords (In Spanish)

Indicate 3 keywords in Times New Roman and Bold No. 10

* Correspondence to Author (example@example.org)
† Researcher contributing as first author.

Instructions for Scientific, Technological and Innovation Publication

Introduction

Text in Times New Roman No.12, single space.

General explanation of the subject and explain why it is important.

What is your added value with respect to other techniques?

Clearly focus each of its features

Clearly explain the problem to be solved and the central hypothesis.

Explanation of sections Article.

## Development of headings and subheadings of the article with subsequent numbers

[Title No.12 in Times New Roman, single spaced and bold]

Products in development No.12 Times New Roman, single spaced.

## Including graphs, figures and tables-Editable

In the article content any graphic, table and figure should be editable formats that can change size, type and number of letter, for the purposes of edition, these must be high quality, not pixelated and should be noticeable even reducing image scale.

[Indicating the title at the bottom with No.10 and Times New Roman Bold]
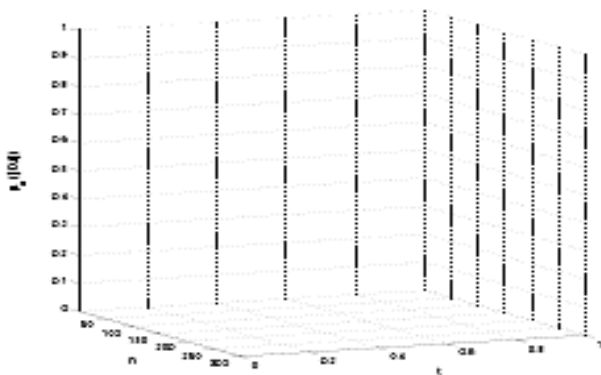
Graphic 1 Title and *Source (in italics)*

Should not be images-everything must be editable.
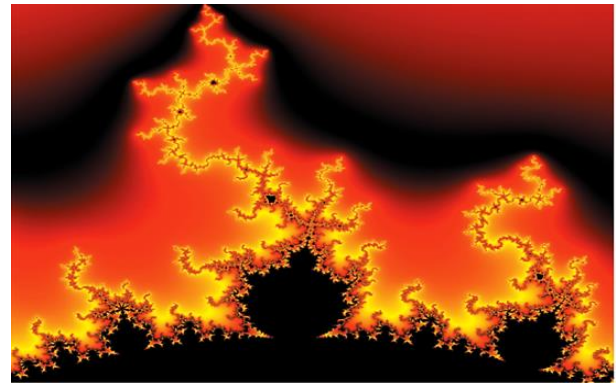
Figure 1 Title and *Source (in italics)*

Should not be images-everything must be editable.

Table 1 Title and *Source (in italics)*

Should not be images-everything must be editable.

Each article shall present separately in **3 folders**: a) Figures, b) Charts and c) Tables in .JPG format, indicating the number and sequential Bold Title.

For the use of equations, noted as follows:

$$Y_{ij} = \alpha + \sum_{h=1}^{r} \beta_h X_{hij} + u_j + e_{ij} \qquad (1)$$

Must be editable and number aligned on the right side.

Methodology

Develop give the meaning of the variables in linear writing and important is the comparison of the used criteria.

Results

The results shall be by section of the article.

Annexes

Tables and adequate sources

Thanks

Indicate if they were financed by any institution, University or company.

Conclusions

Explain clearly the results and possibilities of improvement.

Surname (IN UPPERCASE), Name 1st Author, Surname (IN UPPERCASE), Name 1st Co-author, Surname (IN UPPERCASE), Name 2nd Co-author and Surname (IN UPPERCASE), Name 3rd Co-author. Paper Title ECORFAN Journal- Taiwan. Year [Times New Roman No. 8]

References

Use APA system. Should not be numbered, nor with bullets, however if necessary numbering will be because reference or mention is made somewhere in the Article.

Use Roman Alphabet, all references you have used must be in the Roman Alphabet, even if you have quoted an Article, book in any of the official languages of the United Nations (English, French, German, Chinese, Russian, Portuguese, Italian, Spanish, Arabic), you must write the reference in Roman script and not in any of the official languages.

Technical Specifications

Each article must submit your dates into a Word document (.docx):

Journal Name
Article title
Abstract
Keywords
Article sections, for example:

1. Introduction
2. Description of the method
3. Analysis from the regression demand curve
4. Results
5. Thanks
6. Conclusions
7. References

Author Name (s)
Email Correspondence to Author
References

Intellectual Property Requirements for editing:

- Authentic Signature in Color of <u>Originality Format</u> Author and Co-authors.

- Authentic Signature in Color of the <u>Acceptance Format</u> of Author and Co-authors.

- Authentic Signature in blue colour of the <u>Conflict of Interest Format</u> of Author and Co-authors.

Reservation to Editorial Policy

ECORFAN Journal-Taiwan reserves the right to make editorial changes required to adapt the Articles to the Editorial Policy of the Journal. Once the Article is accepted in its final version, the Journal will send the author the proofs for review. ECORFAN® will only accept the correction of errata and errors or omissions arising from the editing process of the Journal, reserving in full the copyrights and content dissemination. No deletions, substitutions or additions that alter the formation of the Article will be accepted.

Code of Ethics - Good Practices and Declaration of Solution to Editorial Conflicts

Declaration of Originality and unpublished character of the Article, of Authors, on the obtaining of data and interpretation of results, Acknowledgments, Conflict of interests, Assignment of rights and Distribution.

The ECORFAN-Mexico, S.C Management claims to Authors of Articles that its content must be original, unpublished and of Scientific, Technological and Innovation content to be submitted for evaluation.

The Authors signing the Article must be the same that have contributed to its conception, realization and development, as well as obtaining the data, interpreting the results, drafting and reviewing it. The Corresponding Author of the proposed Article will request the form that follows.

Article title:

–   The sending of an Article to ECORFAN Journal-Taiwan emanates the commitment of the author not to submit it simultaneously to the consideration of other series publications for it must complement the Format of Originality for its Article, unless it is rejected by the Arbitration Committee, it may be withdrawn.

–   None of the data presented in this article has been plagiarized or invented. The original data are clearly distinguished from those already published. And it is known of the test in PLAGSCAN if a level of plagiarism is detected Positive will not proceed to arbitrate.

–   References are cited on which the information contained in the Article is based, as well as theories and data from other previously published Articles.

–   The authors sign the Format of Authorization for their Article to be disseminated by means that ECORFAN-Mexico, S.C. In its Holding Taiwan considers pertinent for disclosure and diffusion of its Article its Rights of Work.

–   Consent has been obtained from those who have contributed unpublished data obtained through verbal or written communication, and such communication and Authorship are adequately identified.

–   The Author and Co-Authors who sign this work have participated in its planning, design and execution, as well as in the interpretation of the results. They also critically reviewed the paper, approved its final version and agreed with its publication.

–   No signature responsible for the work has been omitted and the criteria of Scientific Authorization are satisfied.

–   The results of this Article have been interpreted objectively. Any results contrary to the point of view of those who sign are exposed and discussed in the Article.

Copyright and Access

The publication of this Article supposes the transfer of the copyright to ECORFAN-Mexico, SC in its Holding Taiwan for its ECORFAN Journal- Taiwan, which reserves the right to distribute on the Web the published version of the Article and the making available of the Article in This format supposes for its Authors the fulfilment of what is established in the Law of Science and Technology of the United Mexican States, regarding the obligation to allow access to the results of Scientific Research.

Article Title:

Name and Surnames of the Contact Author and the Co-authors	Signature
1.	
2.	
3.	
4.	

Principles of Ethics and Declaration of Solution to Editorial Conflicts

Editor Responsibilities

The Publisher undertakes to guarantee the confidentiality of the evaluation process, it may not disclose to the Arbitrators the identity of the Authors, nor may it reveal the identity of the Arbitrators at any time.

The Editor assumes the responsibility to properly inform the Author of the stage of the editorial process in which the text is sent, as well as the resolutions of Double-Blind Review. The Editor should evaluate manuscripts and their intellectual content without distinction of race, gender, sexual orientation, religious beliefs, ethnicity, nationality, or the political philosophy of the Authors.

The Editor and his editing team of ECORFAN® Holdings will not disclose any information about Articles submitted to anyone other than the corresponding Author.

The Editor should make fair and impartial decisions and ensure a fair Double-Blind Review.

Responsibilities of the Editorial Board

The description of the peer review processes is made known by the Editorial Board in order that the Authors know what the evaluation criteria are and will always be willing to justify any controversy in the evaluation process. In case of Plagiarism Detection to the Article the Committee notifies the Authors for Violation to the Right of Scientific, Technological and Innovation Authorization.

Responsibilities of the Arbitration Committee

The Arbitrators undertake to notify about any unethical conduct by the Authors and to indicate all the information that may be reason to reject the publication of the Articles. In addition, they must undertake to keep confidential information related to the Articles they evaluate.

Any manuscript received for your arbitration must be treated as confidential, should not be displayed or discussed with other experts, except with the permission of the Editor.

The Arbitrators must be conducted objectively, any personal criticism of the Author is inappropriate.

The Arbitrators must express their points of view with clarity and with valid arguments that contribute to the Scientific, Technological and Innovation of the Author.

The Arbitrators should not evaluate manuscripts in which they have conflicts of interest and have been notified to the Editor before submitting the Article for Double-Blind Review.

Responsibilities of the Authors

Authors must guarantee that their articles are the product of their original work and that the data has been obtained ethically.

Authors must ensure that they have not been previously published or that they are not considered in another serial publication.

Authors must strictly follow the rules for the publication of Defined Articles by the Editorial Board.

The authors have requested that the text in all its forms be an unethical editorial behavior and is unacceptable, consequently, any manuscript that incurs in plagiarism is eliminated and not considered for publication.

Authors should cite publications that have been influential in the nature of the Article submitted to arbitration.

Information services

Indexation - Bases and Repositories

RESEARCH GATE (Germany)
GOOGLE SCHOLAR (Citation indices-Google)
MENDELEY (Bibliographic References Manager)
HISPANA (Information and Bibliographic Orientation-Spain)

Publishing Services

Citation and Index Identification H
Management of Originality Format and Authorization
Testing Article with PLAGSCAN
Article Evaluation
Certificate of Double-Blind Review
Article Edition
Web layout
Indexing and Repository
ArticleTranslation
Article Publication
Certificate of Article
Service Billing

Editorial Policy and Management

69 Street. YongHe district, ZhongXin. Taipei-Taiwan. Phones: +52 1 55 6159 2296, +52 1 55 1260 0355, +52 1 55 6034 9181; Email: contact@ecorfan.org www.ecorfan.org

ECORFAN Journal-Taiwan

"Numerical analysis of the hydrodynamic behavior of a magnetoreological fluid"
ORTEGA-ROMERO, Daysi Flor de Liz, ZÚÑIGA-CERROBLANCO, José Luis and HORTELANO-CAPETILLO, Juan Gregorio
Universidad Politécnica de Juventino Rosas

"Automatic blood vessel detection using fractional Hessian matrices"
MARTÍNEZ-JIMÉNEZ, Leonardo, LÓPEZ-LARA, Pedro, FLORES-BALDERAS, Adán and LÓPEZ-HERNÁNDEZ, Juan Manuel
Universidad de Guanajuato

"Use of unstructured meshes for wave height and particles horizontal displacement analysis in central zone Veracruz, Mexico"
AGUILERA-MENDEZ, José María, JUAREZ-TOLEDO, Carlos, MARTINEZ-CARRILLO, Irma and VERA-POPOCA, Roberto Ismael
Universidad Autónoma del Estado de México

"BFO films obtained by Spray Pyrolysis optical and structural analysis"
HERNÁNDEZ-SIMÓN, Zaira Jocelyn, LUNA-LÓPEZ, José Alberto, HERNÁNDEZ-DE LA LUZ, Álvaro David and MENDOZA-CONDE, Gabriel Omar
Benemérita Universidad Autónoma de Puebla

www.ecorfan.org